Barroso, G., Gil, A.J., Ledger, P.D., Mallett, M. and Huerta, A., "A regularised-adaptive Proper Generalised Decomposition implementation for coupled magneto-mechanical problems with application to MRI scanners," to appear in *Computer Methods in Applied Mechanics and Engineering*, Vol 358 (2020).

A regularised-adaptive Proper Generalised Decomposition implementation for coupled magneto-mechanical problems with application to MRI scanners

Guillem Barroso [a], Antonio J. Gil [a], Paul D. Ledger [a], Mike Mallett [b] and Antonio Huerta [c]

(a) Zienkiewicz Centre for Computational Engineering, College of Engineering
Swansea University, Bay Campus, SA1 8EN, United Kingdom
{guillem.barroso, a.j.gil, p.d.ledger}@swansea.ac.uk
(b) Siemens Healthineers, MR Magnet Technology,
Wharf Road, Eynsham, Witney, Oxon OX29 4BP, United Kingdom
michael.mallett@siemens-healthineers.com
(c) Laboratori de Càlcul Numèric (LaCàN), Universitat Politècnica de Catalunya
c/ Jordi Girona 1-3 Edifici C2, 08034, Barcelona, Spain
antonio.huerta@upc.edu

Abstract

Latest developments in high-strength Magnetic Resonance Imaging (MRI) scanners with in-built high resolution, have dramatically enhanced the ability of clinicians to diagnose tumours and rare illnesses. However, their high-strength transient magnetic fields induce unwanted eddy currents in shielding components, which result in fast vibrations, noise, imaging artefacts and, ultimately, heat dissipation, boiling off the helium used to super-cool the magnets. Optimum MRI scanner design requires the capturing of complex electro-magneto-mechanical interactions with high fidelity computational tools. During production cycles, this is known to be extremely expensive due to the large number of configurations that need to be tested. There is an urgent need for the development of new cost-effective methods whereby previously performed computations can be assimilated as training solutions of a surrogate digital twin model to allow for real-time simulations. In this paper, a Reduced Order Modelling technique based on the Proper Generalised Decomposition method is presented for the first time in the context of MRI scanning design, with two distinct novelties. First, the paper derives from scratch the offline higher dimensional parametrised solution process of the coupled electro-magneto-mechanical problem at

hand and, second, a regularised adaptive methodology is proposed for the circumvention of numerical singularities associated with the ill-conditioning of the discrete system in the vicinity of resonant modes. A series of numerical examples are presented in order to illustrate, motivate and demonstrate the validity and flexibility of the considered approach.

Keywords: Magneto-mechanics; coupled problems; *hp*-FEM; medical imaging; MRI scanners; reduced order methods; proper generalised decomposition; real-time simulation.

1 Introduction

Magnetic Resonance Imaging (MRI) scanners are routinely used these days in hospital environments for medical imaging due to their non-intrusive nature [1] and their high performance when imaging fractures [2], joints [3] and soft tissues, such as damaged cartilage [4] or tumours [5]. The underpinning physical principle of an MRI scanner relies on the generation of high-strength magnetic fields through superconducting magnets [6] immersed in a supercooled vessel of liquid helium. A prototypical MRI scanner, see Figure 1, consists of a cryostat with conducting radiation shields that prevent radiation from escaping through and help maintain the supercooled coils at a temperature of approximately 4K [7]. Main coils create a strong uniform static magnetic field that aligns the protons of the hydrogen atoms in the patient's body. The strength of this static magnetic field determines the so-called strength of the magnet, usually between 1.5 and 7 T [8, 9]. Additional gradient coils emit time-varying magnetic pulses that knock the protons out of alignment. When these transient magnetic pulses are turned off , the protons tend to realign differently depending on the type of tissue, sending thus different electric signals which form the patient's medical image [1].

The two main physics interacting in an MRI scanner are electromagnetics and mechanics. It is now well established, from the computational modelling viewpoint, how to independently solve either of them. For instance, for high frequency problems, the displacement currents in Maxwell's equations dominate over the Ohmic currents [10]; but when considering low frequency signals interacting with highly conducting bodies, the eddy current approximation [11–14] can be applied, as in the case of the conducting shields in an MRI scanner. In the context of mechanics, the small deformations assumption for these conducting components is considered to be valid and the theory of linear elasticity to hold [15]. However, the coupling or interaction between both physics introduce extra complexities from the modelling standpoint. First, the interaction of a transient magnetic field with conducting components generates eddy currents which propagate and translate into undesirable deformations and vibrations. These vibrations can, in turn, perturb the surrounding magnetic field. This feedback mechanism between (i) transient magnetic fields, (ii) eddy currents and (iii) mechanical vibrations, results in a fully non-

(a) MRI model MAGNETOM Sola 1.5 T, courtesy of Siemens Healthineers.

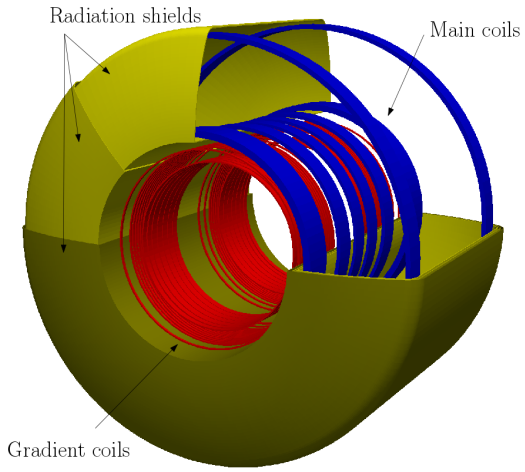

(b) Simplified MRI showing the three main components: main coils, gradient coils and radiation shields.

Figure 1: MRI scanner description.

linear electro-magneto-mechanical problem [16]. This complex coupled effect can yield imaging artefacts [17, 18] as well as disconcerting mechanical vibrations [19], which overall decrease the imaging quality and the lifespan of the MRI scanning equipment.[1] The computational modelling of this problem has been the subject of study of some authors. In [22,23] a low order space-time finite element scheme for the solution of three-dimensional magneto-mechanical problems was presented. In previous work [20, 21, 24] and in search of highly accurate computations, a high order *hp*-finite element software was developed for axisymmetric configurations in conjunction with a stress tensor formulation and a novel linearised approach using an AC-DC splitting, which allows for its time harmonic solution in the frequency domain.

Latest developments in MRI scanners show how manufacturers have oriented their research towards the design and manufacturing of high-strength MRI equipment, with in-built high resolution, capable of dramatically enhance the ability of clinicians to diagnose tumours and rare illnesses [25]. Yet according to Siemens Healthineers, the design phase of an MRI scanner is still far from being an automatised process. Indeed, "*...the magnet was four years in the making, two of which were spent in scientific research...*" according to their design lead team [26]. A design bottleneck relates to the large number of configurations that need to be tested (i.e. variable frequency, conductivity, shield thicknesses) making the production cycle extremely expensive from the computational standpoint. There is an urgent need for the development of new cost-effective modelling techniques whereby

[1] Note that the consideration of the acoustics phenomenon has been neglected in this study. The interested reader is referred to our previous work [20, 21] for all the necessary details of a fully coupled acousto-electro-magneto-mechanical problem.

previously performed computations can be assimilated as training solutions of a surrogate digital twin model to allow for real-time simulations, thus minimising human intervention.

In this sense, Reduced Order Modelling (ROM) techniques have recently gained momentum to help speed up the multiple-query stage of the design optimisation process via real-time approximations of the so-called full order solution [27, 28]. Within the ample spectrum of ROM methods, so-called *a posteriori* ROM relies on a previously known (or pre-computed) approximation basis (reduced basis [29, 30]) for the full order solution, typically obtained through the calculation of key snapshots that can potentially describe the general response of the system, as in the Proper Orthogonal Decomposition (POD) method [31, 32]. Alternatively, *a priori* ROM methods, such as the Proper Generalised Decomposition (PGD) method [33], do not require any previously stored information of the system. They formulate first, a higher-dimensional parametric offline stage solution and, subsequently, in the online stage, a simple interpolation of this parametric solution is carried out, being thus able to achieve fast (real-time) simulations. This PGD methodology has been successfully implemented in numerous applications, such as Helmholtz based problems [34, 35], solid mechanics [36], power distribution systems [37], flow problems [38, 39], thermal problems [40, 41], degenerated 3D domains such as plates and shells [42] and also with geometrical parametrisations for heat problems [43].

The main aim of this paper is to formulate and develop, for the first time, a PGD ROM computational framework for the design phase of the next generation of MRI scanners (>7T), speeding up the optimisation workflow and its resulting manufacture. In this work, the external exciting frequency will be considered as an additional parameter of our offline higher-dimensional parametric solution permitting frequency spectra for kinetic energy and dissipated Ohmic power to be efficiently queried in real time in the online stage. With this in mind, two main novelties will be put forward in this work. First, the development from scratch of the PGD ROM methodology for the coupled electro-magento-mechanical problem at hand and, second, a regularised adaptive methodology proposed for the circumvention of numerical singularities associated with the ill-conditioning of the PGD system in the vicinity of resonant modes.

The paper is organised as follows; in Section 2 the two physics governing the behaviour of the problem are described together with the appropriate set of transmission, boundary and initial conditions. Section 3 presents the computational treatment of the problem, including a linearisation approach and the axisymmetric assumption. The fundamentals of the PGD method are briefly presented in Section 4, where the angular frequency is considered as the extra parameter used in the higher-dimensional parametric offline solution. A regularised-adaptive PGD methodology is then described in Section 5 to overcome the presence of numerical singularities in the resonance region. The paper finishes with Section 6, where a set of numerical examples are presented in order to demonstrate the validity, applicability and versatility of the proposed PGD technique.

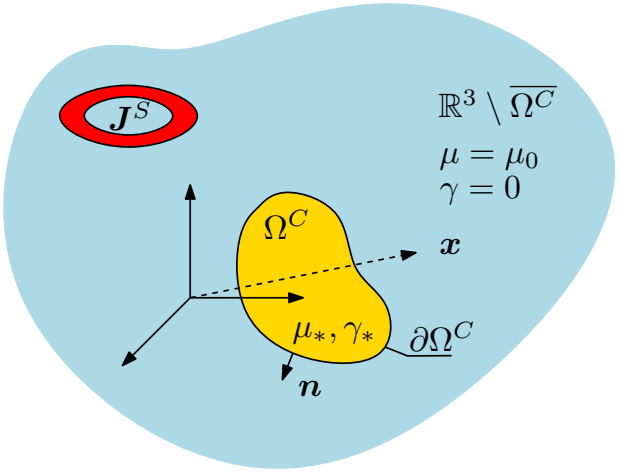

Figure 2: Conducting component Ω^C (with magnetic permeability $\mu = \mu_*$ and electrical conductivity $\gamma = \gamma_*$) in a non-conducting three dimensional space $\mathbb{R}^3 \setminus \overline{\Omega^C}$ (with $\mu = \mu_0$ and $\gamma = 0$). Problem excited by a current source $\boldsymbol{J}^S$ acting in a series of coils.

2 Physics description

In the presence of moving components (within a computational electromagnetic domain), it is customary to establish a reference position $\boldsymbol{X}$ and a time-dependent ($t \in [0, T]$) mapping $\boldsymbol{\phi}$ that links this reference state to the current position $\boldsymbol{\phi}(\boldsymbol{X}, t)$. Adopting a Lagrangian viewpoint [44], the Lagrangian electromagnetic fields $\boldsymbol{H}_0$, $\boldsymbol{E}_0$ and $\boldsymbol{B}_0$ are used, which denote the magnetic field intensity, the electric field intensity and the magnetic flux density, respectively. In addition, the following considerations are made: (1) both the eddy current approximation and the constitutive laws for electromagnetics are applied in the Eulerian setting and, then, the simplified Maxwell equations are transformed to the Lagrangian description; (2) for small displacements $\boldsymbol{u}$ (although not necessarily small velocities or accelerations), Total and Updated Lagrangian descriptions coincide; (3) a vector potential formulation $\boldsymbol{A}$ is used where the gauging of the electromagnetic problem is applied to the already Lagrangian eddy current model; (4) the Cauchy stress tensor is comprised of a mechanical $\boldsymbol{\sigma}^m(\boldsymbol{u})$ and an electromagnetic interaction Maxwell stress component $\boldsymbol{\sigma}^e(\boldsymbol{A})$ defined in terms of $\boldsymbol{B}_0$. Thus, the non-linear coupled magneto-mechanical problem, see Figure 2, can be summarised in strong form as follows: Find $(\boldsymbol{A}, \boldsymbol{u})(t) \in (\mathbb{R}^3 \times \mathbb{R}^3)[0, T]$ such that

$$\operatorname{curl}(\mu^{-1} \operatorname{curl} \boldsymbol{A}) + \gamma \frac{d\boldsymbol{A}}{dt} = \boldsymbol{J}^S \qquad \text{in } \mathbb{R}^3, \tag{1a}$$

$$\operatorname{div} \boldsymbol{A} = 0 \qquad \text{in } \mathbb{R}^3 \setminus \overline{\Omega^C}, \tag{1b}$$

$$\operatorname{div}(\boldsymbol{\sigma}^m(\boldsymbol{u}) + \boldsymbol{\sigma}^e(\boldsymbol{A})) = \rho \frac{d^2\boldsymbol{u}}{dt^2} \qquad \text{in } \Omega^C, \tag{1c}$$

$$\boldsymbol{\sigma}^m(\boldsymbol{u}) := \boldsymbol{\mathcal{C}} : \boldsymbol{\varepsilon}(\boldsymbol{u}) \qquad \text{in } \Omega^C, \tag{1d}$$

$$\boldsymbol{\sigma}^e(\boldsymbol{A}) := \mu^{-1}\Big((\operatorname{curl}\boldsymbol{A}) \otimes (\operatorname{curl}\boldsymbol{A}) - \frac{1}{2}|\operatorname{curl}\boldsymbol{A}|^2\boldsymbol{I}\Big) \qquad \text{in } \Omega^C, \tag{1e}$$

$$\boldsymbol{A} = O\big(|\boldsymbol{x}|^{-1}\big) \qquad \text{as } |\boldsymbol{x}| \to \infty, \tag{1f}$$

$$\boldsymbol{u} = \boldsymbol{u}_D \qquad \text{on } \partial\Omega^C_D, \tag{1g}$$

$$\boldsymbol{n} \times [\boldsymbol{A}]_{\partial\Omega^C} = \boldsymbol{0} \qquad \text{on } \partial\Omega^C, \tag{1h}$$

$$\boldsymbol{n} \times [\mu^{-1}\operatorname{curl}\boldsymbol{A}]_{\partial\Omega^C} = \boldsymbol{0} \qquad \text{on } \partial\Omega^C, \tag{1i}$$

$$\big(\boldsymbol{\sigma}^m(\boldsymbol{u}) + \boldsymbol{\sigma}^e(\boldsymbol{A})\big)\big|^-_{\partial\Omega^C}\boldsymbol{n} = \boldsymbol{\sigma}^e(\boldsymbol{A})\big|^+_{\partial\Omega^C}\boldsymbol{n} \qquad \text{on } \partial\Omega^C, \tag{1j}$$

$$\boldsymbol{A}|_{t=0} = \boldsymbol{0} \qquad \text{in } \mathbb{R}^3, \tag{1k}$$

$$\boldsymbol{u}|_{t=0} = \left.\frac{d\boldsymbol{u}}{dt}\right|_{t=0} = \boldsymbol{0} \qquad \text{in } \Omega^C, \tag{1l}$$

where μ is the magnetic permeability, γ is the electrical conductivity and ρ the material density. The current source is denoted by $\boldsymbol{J}^S$, $\boldsymbol{I}$ is the second order identity tensor, $\boldsymbol{x}$ represents the position vector, $\boldsymbol{n}$ denotes the outward normal vector (pointing from the conducting to the non-conducting side), $\boldsymbol{\varepsilon} := \big(\nabla\boldsymbol{u} + (\nabla\boldsymbol{u})^T\big)/2$ is the small strain tensor and $\boldsymbol{\mathcal{C}}$ is the fourth order elasticity tensor dependent upon the Lamé parameters. Note that $\overline{\Omega^C} := \Omega^C \cup \partial\Omega^C$ and hence the overbar denotes the closure of Ω^C, later we will also use the overbar to denote the complex conjugate, however, it should be clear from the context as to which definition applies. The $\boldsymbol{A}$-based formulation [14] is used in (1) with $\boldsymbol{B}_0 = \operatorname{curl}\boldsymbol{A}$. In (1a), (1c) and (1l), $\frac{d}{dt}$ represents the total (material) derivative. The notation $[\cdot]_{\partial\Omega^C}$ appearing in (1h) and (1i) indicates the jump on the interface $\partial\Omega^C$, namely $[\cdot]_{\partial\Omega^C} := (\cdot)|^+_{\partial\Omega^C} - (\cdot)|^-_{\partial\Omega^C}$, where $(\cdot)|^+_{\partial\Omega^C}$ and $(\cdot)|^-_{\partial\Omega^C}$ denote the non-conducing and conducting sides, respectively, on the interface $\partial\Omega^C$.

The equations governing the electromagnetic problem (1a)-(1b) describe the so-called eddy current approximation of the general Maxwell's equations. The mechanical problem is represented by the conservation of linear momentum (1c) together with the definitions of the Cauchy (1d) and the Maxwell (1e) stress tensors. The decay of the vector potential field is shown in (1f) and the imposed displacements on the Dirichlet part of the boundary are shown on (1g). Interface conditions (1h)-(1j) represent the continuity on the tangential component of $\boldsymbol{A}$ and $\boldsymbol{H}_0$, together with the continuity of tractions, respectively. Finally, the initial conditions (1k)-(1l) are added for the well-posedness of the problem. After solution of (1), the actual Eulerian electric and magnetic quantities of interest can be recovered as[2]

$$\boldsymbol{E} = -\frac{d\boldsymbol{A}}{dt} + \boldsymbol{B}_0 \times \frac{d\boldsymbol{u}}{dt} \qquad \text{in } \Omega^C, \tag{2a}$$

$$\boldsymbol{H} = \mu^{-1}\boldsymbol{B}_0 = \mu^{-1}\operatorname{curl}\boldsymbol{A} \qquad \text{in } \mathbb{R}^3. \tag{2b}$$

[2] $\boldsymbol{H} = \boldsymbol{H}_0$ is assumed due to low electric permittivities.

3 Weak formulation and approximating assumptions

Following previous work in [20, 21, 24], this Section briefly recalls the approximating assumptions introduced to lead from the strong form (1)-(2) to the weak form. First, a linearisation methodology is introduced, where an AC-DC splitting of the problem is performed, which enables the transformation of the transient problem from the time to the (more efficient) frequency domain. Second, the axisymmetric approximation is described and, finally, an augmented (extended) weak formulation is presented for both electromagnetic and mechanical problems, including the parametric domain of exciting frequencies as part of the augmented (extended) solution domain.

3.1 Linearisation methodology

Since the operating of an MRI scanner involves the application of a strong static magnetic field (DC) and superimposed small time-dependent magnetic fields (AC), it is advocated in [45–49] for a linearisation of the governing equations about the static solution, resulting in a linear transient problem. In addition, in [21], a linearised frequency approach is discussed and assessed against the linearised and the non-linear time dependent formulations, obtaining an excellent agreement for this particular application yet with considerably less computational effort. With this in mind, the first step is the split of the current source as

$$\boldsymbol{J}^{S}(t) = \boldsymbol{J}^{DC} + \boldsymbol{J}^{AC}(t), \tag{3}$$

into a static (DC) field $\boldsymbol{J}^{DC}$ generated by the main coils and a time-depending (AC) field $\boldsymbol{J}^{AC}(t)$ generated by the gradient coils. The linearisation of the transient problem can be found in [16, 20], where a time-harmonic representation of the time-dependent fields is introduced by assuming that they can be written in terms of a single frequency ω as follows

$$\boldsymbol{A}^{AC}(t) \rightarrow \boldsymbol{\mathcal{A}}^{AC} e^{\mathrm{i}\omega t}, \tag{4a}$$
$$\boldsymbol{u}^{AC}(t) \rightarrow \boldsymbol{\mathcal{U}}^{AC} e^{\mathrm{i}\omega t}, \tag{4b}$$
$$\boldsymbol{J}^{AC}(t) \rightarrow \boldsymbol{\mathcal{J}}^{AC} e^{\mathrm{i}\omega t}, \tag{4c}$$

where $\mathrm{i} := \sqrt{-1}$ and $\omega = 2\pi f$ represents the angular frequency of the harmonic excitation, with f the temporal frequency of the problem. The angular frequency is selected within a prescribed interval of interest as $\omega \in \Omega_\omega = (0, \omega_{max}]$ where ω_{max} is the maximum frequency considered. Note that $\boldsymbol{\mathcal{A}}^{AC}$, $\boldsymbol{\mathcal{U}}^{AC}$ and $\boldsymbol{\mathcal{J}}^{AC}$ denote the complex amplitudes of their respective time-dependent fields. The linearisation consists on formulating a static (DC) problem whose solution is used as the initial condition for the transient (AC) problem, see Figure 3. The solution of the overall problem is thus obtained as the sum of both DC and AC solutions as

$$\boldsymbol{A}(t) = \boldsymbol{A}^{DC} + \mathrm{Re}\left(\boldsymbol{\mathcal{A}}^{AC} e^{\mathrm{i}\omega t}\right), \tag{5a}$$
$$\boldsymbol{u}(t) = \boldsymbol{u}^{DC} + \mathrm{Re}\left(\boldsymbol{\mathcal{U}}^{AC} e^{\mathrm{i}\omega t}\right), \tag{5b}$$

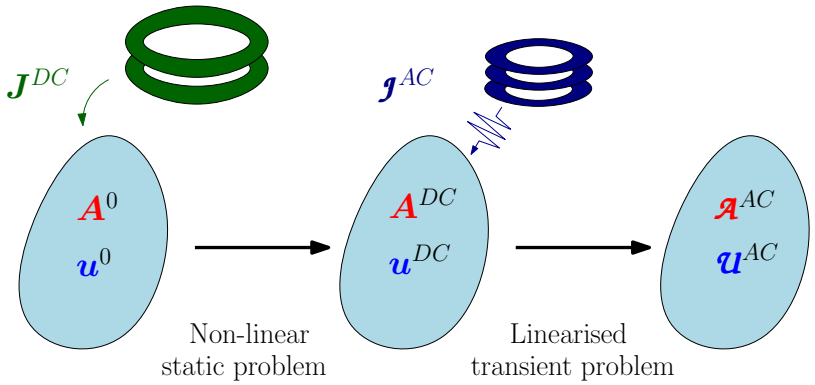

Figure 3: Linearisation process; initial state excited through static current source $\boldsymbol{J}^{DC}$. Solution of static problem is used as the initial state for the transient problem with time-harmonic current source $\boldsymbol{\mathcal{J}}^{AC}$.

where $\mathrm{Re}\,(\cdot)$ denotes the real part of a given field.

3.1.1 DC problem

The non-linear (due to the Maxwell stress tensor $\boldsymbol{\sigma}^e(\boldsymbol{A}^{DC})$) static problem is defined through the following strong from: Find $(\boldsymbol{A}^{DC}, \boldsymbol{u}^{DC}) \in (\mathbb{R}^3 \times \mathbb{R}^3)$ such that

$$\begin{aligned}
\operatorname{curl}(\mu^{-1} \operatorname{curl} \boldsymbol{A}^{DC}) &= \boldsymbol{J}^{DC} && \text{in } \mathbb{R}^3, && (6a)\\
\operatorname{div} \boldsymbol{A}^{DC} &= 0 && \text{in } \mathbb{R}^3, && (6b)\\
\operatorname{div}\left(\boldsymbol{\sigma}^m(\boldsymbol{u}^{DC}) + \boldsymbol{\sigma}^e(\boldsymbol{A}^{DC})\right) &= \boldsymbol{0} && \text{in } \Omega^C, && (6c)\\
\boldsymbol{A}^{DC} &= O\left(|\boldsymbol{x}|^{-1}\right) && \text{as } |\boldsymbol{x}| \to \infty, && (6d)\\
\boldsymbol{u}^{DC} &= \boldsymbol{u}_D^{DC} && \text{on } \partial\Omega_D^C, && (6e)\\
\boldsymbol{n} \times [\boldsymbol{A}^{DC}]_{\partial\Omega^C} &= \boldsymbol{0} && \text{on } \partial\Omega^C, && (6f)\\
\boldsymbol{n} \times [\mu^{-1} \operatorname{curl} \boldsymbol{A}^{DC}]_{\partial\Omega^C} &= \boldsymbol{0} && \text{on } \partial\Omega^C, && (6g)\\
\left(\boldsymbol{\sigma}^m(\boldsymbol{u}^{DC}) + \boldsymbol{\sigma}^e(\boldsymbol{A}^{DC})\right)\big|^-_{\partial\Omega^C}\boldsymbol{n} &= \boldsymbol{\sigma}^e(\boldsymbol{A}^{DC})\big|^+_{\partial\Omega^C}\boldsymbol{n} && \text{on } \partial\Omega^C. && (6h)
\end{aligned}$$

3.1.2 AC problem

The governing equations for the linearised transient problem are derived in [16] and the strong form is defined as: Find $(\boldsymbol{\mathcal{A}}^{AC}, \boldsymbol{\mathcal{U}}^{AC}) \in (\mathbb{C}^3 \times \mathbb{C}^3)$ such that

$$\begin{aligned}
\operatorname{curl}(\mu^{-1} \operatorname{curl} \boldsymbol{\mathcal{A}}^{AC}) + \mathrm{i}\omega\gamma\boldsymbol{\mathcal{A}}^{AC} &= \boldsymbol{\mathcal{J}}^{AC} && \text{in } \mathbb{R}^3, && (7a)\\
\operatorname{div} \boldsymbol{\mathcal{A}}^{AC} &= 0 && \text{in } \mathbb{R}^3 \setminus \overline{\Omega^C}, && (7b)
\end{aligned}$$

$$
\begin{aligned}
\operatorname{div}\left(\boldsymbol{\sigma}^m(\boldsymbol{\mathcal{U}}^{AC}) + \mu^{-1}\boldsymbol{T}(\boldsymbol{A}^{DC}, \boldsymbol{\mathcal{A}}^{AC})\right) &= -\rho\omega^2\boldsymbol{\mathcal{U}}^{AC} && \text{in } \Omega^C, && \text{(7c)}\\
\boldsymbol{\mathcal{A}}^{AC} &= O\big(|\boldsymbol{x}|^{-1}\big) && \text{as } |\boldsymbol{x}| \to \infty, && \text{(7d)}\\
\boldsymbol{\mathcal{U}}^{AC} &= \boldsymbol{\mathcal{U}}_D^{AC} && \text{on } \partial\Omega_D^C, && \text{(7e)}\\
\boldsymbol{n} \times [\boldsymbol{\mathcal{A}}^{AC}]_{\partial\Omega^C} &= \boldsymbol{0} && \text{on } \partial\Omega^C, && \text{(7f)}\\
\boldsymbol{n} \times [\mu^{-1}\operatorname{curl}\boldsymbol{\mathcal{A}}^{AC}]_{\partial\Omega^C} &= \boldsymbol{0} && \text{on } \partial\Omega^C, && \text{(7g)}\\
\left(\boldsymbol{\sigma}^m(\boldsymbol{\mathcal{U}}^{AC}) + \mu^{-1}\boldsymbol{T}(\boldsymbol{A}^{DC}, \boldsymbol{\mathcal{A}}^{AC})\right)\big|^-_{\partial\Omega^C}\boldsymbol{n} &= \mu^{-1}\boldsymbol{T}(\boldsymbol{A}^{DC}, \boldsymbol{\mathcal{A}}^{AC})\big|^+_{\partial\Omega^C}\boldsymbol{n} && \text{on } \partial\Omega^C, && \text{(7h)}
\end{aligned}
$$

where in (7c) and (7h) the linearised electromagnetic stress tensor is introduced and defined as

$$
\begin{aligned}
\mu^{-1}\boldsymbol{T}(\boldsymbol{A}^{DC}, \boldsymbol{\mathcal{A}}^{AC}) := \mu^{-1}\big(&(\operatorname{curl}\boldsymbol{A}^{DC}) \otimes (\operatorname{curl}\boldsymbol{\mathcal{A}}^{AC}) + (\operatorname{curl}\boldsymbol{\mathcal{A}}^{AC}) \otimes (\operatorname{curl}\boldsymbol{A}^{DC})\\
&- (\operatorname{curl}\boldsymbol{A}^{DC} \cdot \operatorname{curl}\boldsymbol{\mathcal{A}}^{AC})\boldsymbol{I}\big).
\end{aligned} \qquad (8)
$$

Once the linearised transient problem (7) is solved, the Eulerian electric and magnetic AC fields can be computed as

$$
\begin{aligned}
\boldsymbol{\mathcal{E}}^{AC} &= -\mathrm{i}\omega\boldsymbol{\mathcal{A}}^{AC} + \mathrm{i}\omega\boldsymbol{B}_0^{DC} \times \boldsymbol{\mathcal{U}}^{AC} && \text{in } \Omega^C, && \text{(9a)}\\
\boldsymbol{\mathcal{H}}^{AC} &= \mu^{-1}\boldsymbol{\mathcal{B}}_0^{AC} = \mu^{-1}\operatorname{curl}\boldsymbol{\mathcal{A}}^{AC} && \text{in } \mathbb{R}^3. && \text{(9b)}
\end{aligned}
$$

Finally, the complete time-dependent solution of the problem (5) can be written as

$$
\begin{aligned}
\boldsymbol{E} &= \operatorname{Re}\left(\boldsymbol{\mathcal{E}}^{AC}e^{\mathrm{i}\omega t}\right) = \operatorname{Re}\left((-\mathrm{i}\omega\boldsymbol{\mathcal{A}}^{AC} + \mathrm{i}\omega\boldsymbol{B}_0^{DC} \times \boldsymbol{\mathcal{U}}^{AC})e^{\mathrm{i}\omega t}\right) && \text{in } \Omega^C, && \text{(10a)}\\
\boldsymbol{H} &= \boldsymbol{H}^{DC} + \operatorname{Re}\left(\boldsymbol{\mathcal{H}}^{AC}e^{\mathrm{i}\omega t}\right) = \mu^{-1}\Big(\operatorname{curl}\boldsymbol{A}^{DC} + \operatorname{Re}\left((\operatorname{curl}\boldsymbol{\mathcal{A}}^{AC})e^{\mathrm{i}\omega t}\right)\Big) && \text{in } \mathbb{R}^3. && \text{(10b)}
\end{aligned}
$$

Note that (10) is the linearised time harmonic version of (2).

3.2 Axisymmetric weak formulation

An axisymmetric $\{r, \phi, z\}$ representation is assumed when deriving the weak forms of above strong forms (6)-(7) and the problem is formulated in the meridian two-dimensional plane Ω_p as shown in Figure 4. The unbounded domain is truncated at a finite distance away from the conducting embedded domain Ω_p^C and the decay conditions for $\boldsymbol{A}^{DC}$ and $\boldsymbol{\mathcal{A}}^{AC}$ apply. In addition, the transient current source is represented as $\boldsymbol{\jmath}^{AC}(r, \phi, z) = \jmath_\phi^S(r, z)\boldsymbol{e}_\phi$ and, thus, the solution variables become

$$
\begin{aligned}
\boldsymbol{\mathcal{A}}^{AC} &= r\mathcal{A}_\phi(r, z)\boldsymbol{e}_\phi, && \text{(11a)}\\
\boldsymbol{\mathcal{U}}^{AC} &= \boldsymbol{\mathcal{U}} = r\mathcal{U}_r(r, z)\boldsymbol{e}_r + \mathcal{U}_z(r, z)\boldsymbol{e}_z, && \text{(11b)}
\end{aligned}
$$

where the upper index AC in the fields $\{\mathcal{A}_\phi, \boldsymbol{\mathcal{U}}\}$ is dropped for simplicity and $\boldsymbol{e}_r$, $\boldsymbol{e}_\phi$ and $\boldsymbol{e}_z$ are the unit normal vectors in the r, ϕ and z directions, respectively. In addition, solution

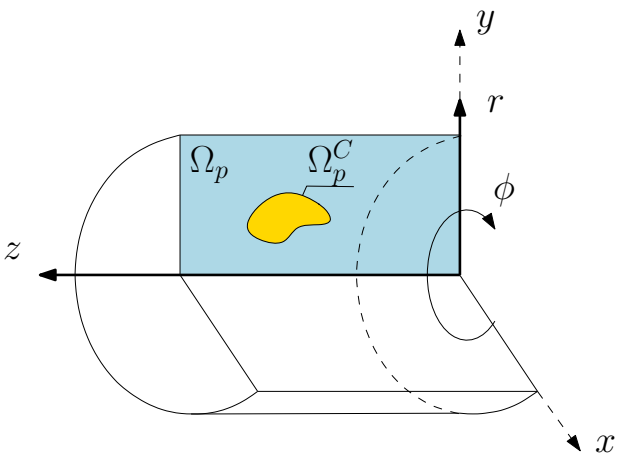

Figure 4: Axisymmetric $\{r, \phi, z\}$ representation of the problem; a conducting component Ω_p^C in a non-conducting domain Ω_p.

fields are scaled in order to avoid singularities along the $r = 0$ axis. In what follows, the axisymmetric AC weak form of problem (7) is presented, as this will form the basis of our frequency (ω) based Proper Generalised Decomposition (PGD) method. Notice that, although the solution to the DC stage is still required, this is independent of the PGD parameter of interest, namely, the frequency ω, and so it is omitted and the reader is referred to [16, 24] for further details.

3.2.1 Electromagnetics

The augmented axisymmetric weak form of the electromagnetic problem is formulated in a higher-dimensional space-frequency space as: Find $\mathcal{A}_\phi \in \mathcal{X}(\mathcal{A}_{\phi,D})$ such that

$$\mathcal{W}_K^{AA}(\mathcal{A}_\phi, \delta\mathcal{A}_\phi) + \mathrm{i}\mathcal{W}_C^{AA}(\mathcal{A}_\phi, \delta\mathcal{A}_\phi) = \mathcal{S}^A(\delta\mathcal{A}_\phi) \qquad \forall \delta\mathcal{A}_\phi \in \mathcal{X}(0), \tag{12}$$

where

$$\mathcal{W}_K^{AA}(a, b) := \int_{\Omega_\omega} W_K^{AA}(a, b)\,\mathrm{d}\omega, \tag{13a}$$

$$\mathcal{W}_C^{AA}(a, b) := \int_{\Omega_\omega} \omega W_C^{AA}(a, b)\,\mathrm{d}\omega, \tag{13b}$$

$$\mathcal{S}^A(b) := \int_{\Omega_\omega} S^A(b)\,\mathrm{d}\omega, \tag{13c}$$

with

$$W_K^{AA}(a, b) := \int_{\Omega_p} \frac{\mu^{-1}}{r} \nabla_p(r^2 a) \cdot \nabla_p(r^2 \bar{b})\,\mathrm{d}\Omega, \tag{14a}$$

$$W_C^{AA}(a, b) := \int_{\Omega_p^C} \gamma a \bar{b} r^3\,\mathrm{d}\Omega, \tag{14b}$$

$$S^A(b) := \int_{\Omega_p} \jmath_\phi^S \overline{b} r^2 \, \mathrm{d}\Omega, \tag{14c}$$

where $(\overline{\cdot})$ now denotes the complex conjugate of a given field and

$$\mathcal{X}(0) := \{\mathcal{A}_\phi : \mathcal{A}_\phi \in H^1(\Omega_p \times \Omega_\omega), \mathcal{A}_\phi = \mathcal{A}_{\phi,D} \text{ on } \partial\Omega_{p,D} \times \Omega_\omega\}, \tag{15}$$

where $\partial\Omega_{p,D}$ is the Dirichlet part of the electromagnetic boundary and the gradient of the scalar potential in the meridian plane is defined as $\nabla_p \mathcal{A}_\phi := \frac{\partial \mathcal{A}_\phi}{\partial r} \boldsymbol{e}_r + \frac{\partial \mathcal{A}_\phi}{\partial z} \boldsymbol{e}_z$ [16]. Note that the angular frequency $\omega \in \Omega_\omega$ has been considered as an extra (parametric) dimension in the augmented weak form (12) and this is emphasised by stating $\mathcal{A}_\phi = \mathcal{A}_\phi(r, z, \omega)$.

3.2.2 Mechanics in embedded conductors

The augmented axisymmetric weak form of the mechanic problem is formulated in a higher-dimensional space-frequency space as: Find $\boldsymbol{u} \in \mathcal{Y}(\boldsymbol{u}_D)$ such that

$$\mathcal{W}_K^{uu}(\boldsymbol{u}, \delta\boldsymbol{u}) + \mathcal{W}_K^{uA}(A_\phi, \delta\boldsymbol{u}) - \mathcal{W}_M^{uu}(\boldsymbol{u}, \delta\boldsymbol{u}) = 0 \qquad \forall \delta\boldsymbol{u} \in \mathcal{Y}(\boldsymbol{0}), \tag{16}$$

where

$$\mathcal{W}_K^{uu}(\boldsymbol{a}, \boldsymbol{b}) := \int_{\Omega_\omega} W_K^{uu}(\boldsymbol{a}, \boldsymbol{b}) \, \mathrm{d}\omega, \tag{17a}$$

$$\mathcal{W}_K^{uA}(a, \boldsymbol{b}) := \int_{\Omega_\omega} W_K^{uA}(a, \boldsymbol{b}) \, \mathrm{d}\omega, \tag{17b}$$

$$\mathcal{W}_M^{uu}(\boldsymbol{a}, \boldsymbol{b}) := \int_{\Omega_\omega} \omega^2 W_M^{uu}(\boldsymbol{a}, \boldsymbol{b}) \, \mathrm{d}\omega, \tag{17c}$$

with

$$W_K^{uu}(\boldsymbol{a}, \boldsymbol{b}) := \int_{\Omega_p^C} \boldsymbol{\sigma}^m(\boldsymbol{a}) : \nabla\overline{\boldsymbol{b}} \, r \, \mathrm{d}\Omega, \tag{18a}$$

$$W_K^{uA}(a, \boldsymbol{b}) := \int_{\Omega_p^C} \mu^{-1} T(A_\phi^{DC}, a) : \nabla\overline{\boldsymbol{b}} \, r \, \mathrm{d}\Omega - \int_{\partial\Omega_p^{C,N}} \mu_0^{-1} T(A_\phi^{DC}, a)\big|^+ \boldsymbol{n} \cdot \overline{\boldsymbol{b}} \, r \, \mathrm{d}S, \tag{18b}$$

$$W_M^{uu}(\boldsymbol{a}, \boldsymbol{b}) := \int_{\Omega_p^C} \rho \boldsymbol{a} \cdot \overline{\boldsymbol{b}} \, r \, \mathrm{d}\Omega. \tag{18c}$$

Similarly as above, the frequency $\omega \in \Omega_\omega$ has been considered in the solution $\boldsymbol{u} = \boldsymbol{u}(r, z, \omega)$ and

$$\mathcal{Y}(\boldsymbol{u}_D) := \{\boldsymbol{u} : \boldsymbol{u} \in (H^1(\Omega_p^C \times \Omega_\omega))^2, \boldsymbol{u} = \boldsymbol{u}_D \text{ on } \partial\Omega_{p,D}^C \times \Omega_\omega\}, \tag{19}$$

with $\partial\Omega_{p,D}^C$ denoting the Dirichlet part of the mechanical boundary.

3.2.3 Coupled magneto-mechanics

Addition of (12) and (16) and introduction of the combined unknown field $\boldsymbol{q} = \boldsymbol{q}(r, z, \omega)$ defined as $\boldsymbol{q} = \begin{bmatrix} \mathcal{A}_\phi & \boldsymbol{u}^T \end{bmatrix}^T$ leads to the augmented higher-dimensional space-frequency weak form of the coupled magneto-mechanical formulation: Find $\boldsymbol{q} \in \mathcal{X}(\mathcal{A}_{\phi,D}) \times \mathcal{Y}(\boldsymbol{u}_D)$ such that

$$\mathcal{W}_K(\boldsymbol{q}, \delta\boldsymbol{q}) + \mathrm{i}\mathcal{W}_C(\boldsymbol{q}, \delta\boldsymbol{q}) - \mathcal{W}_M(\boldsymbol{q}, \delta\boldsymbol{q}) = \mathcal{S}(\delta\boldsymbol{q}) \qquad \forall \delta\boldsymbol{q} \in \mathcal{X}(0) \times \mathcal{Y}(0), \tag{20}$$

where

$$\mathcal{W}_K(\boldsymbol{q}, \delta\boldsymbol{q}) := \mathcal{W}_K^{AA}(\mathcal{A}_\phi, \delta\mathcal{A}_\phi) + \mathcal{W}_K^{uu}(\boldsymbol{u}, \delta\boldsymbol{u}) + \mathcal{W}_K^{uA}(\mathcal{A}_\phi, \delta\boldsymbol{u}), \tag{21a}$$
$$\mathcal{W}_C(\boldsymbol{q}, \delta\boldsymbol{q}) := \mathcal{W}_C^{AA}(\mathcal{A}_\phi, \delta\mathcal{A}_\phi), \tag{21b}$$
$$\mathcal{W}_M(\boldsymbol{q}, \delta\boldsymbol{q}) := \mathcal{W}_M^{uu}(\boldsymbol{u}, \delta\boldsymbol{u}), \tag{21c}$$
$$\mathcal{S}(\delta\boldsymbol{q}) := \mathcal{S}^A(\delta\mathcal{A}_\phi). \tag{21d}$$

Remark 1. *As it will be seen, the additional formulation of the classical weak form for the coupled problem will be proven to be very useful. In this case, the solution field $\boldsymbol{q}$ is only considered to be Ω_p space varying as $\boldsymbol{q} = \boldsymbol{q}(r, z)$ and, hence, the so-called two-dimensional space weak form of the problem is formulated as: Find $\boldsymbol{q} \in X(\mathcal{A}_{\phi,D}) \times Y(\boldsymbol{u}_D)$ such that*

$$W_K(\boldsymbol{q}, \delta\boldsymbol{q}) + \mathrm{i}\omega W_C(\boldsymbol{q}, \delta\boldsymbol{q}) - \omega^2 W_M(\boldsymbol{q}, \delta\boldsymbol{q}) = S(\delta\boldsymbol{q}) \qquad \forall \delta\boldsymbol{q} \in X(0) \times Y(\boldsymbol{0}), \tag{22}$$

where

$$W_K(\boldsymbol{q}, \delta\boldsymbol{q}) := W_K^{AA}(\mathcal{A}_\phi, \delta\mathcal{A}_\phi) + W_K^{uu}(\boldsymbol{u}, \delta\boldsymbol{u}) + W_K^{uA}(\mathcal{A}_\phi, \delta\boldsymbol{u}), \tag{23a}$$
$$W_C(\boldsymbol{q}, \delta\boldsymbol{q}) := W_C^{AA}(\mathcal{A}_\phi, \delta\mathcal{A}_\phi), \tag{23b}$$
$$W_M(\boldsymbol{q}, \delta\boldsymbol{q}) := W_M^{uu}(\boldsymbol{u}, \delta\boldsymbol{u}), \tag{23c}$$
$$S(\delta\boldsymbol{q}) := S^A(\delta\mathcal{A}_\phi), \tag{23d}$$

with

$$X(0) := \{\mathcal{A}_\phi : \mathcal{A}_\phi \in H^1(\Omega_p), \mathcal{A}_\phi = \mathcal{A}_{\phi,D} \ \ on \ \partial\Omega_p\}, \tag{24a}$$
$$Y(\boldsymbol{u}_D) := \{\boldsymbol{u} : \boldsymbol{u} \in (H^1(\Omega_p^C))^2, \boldsymbol{u} = \boldsymbol{u}_D \ \ on \ \partial\Omega_{p,D}^C\}. \tag{24b}$$

4 The frequency based Proper Generalised Decomposition method

In this Section, the Proper Generalised Decomposition (PGD) method is presented for the coupled magneto-mechanical problem (20), where a multi-dimensional parametric solution $\boldsymbol{q} = \boldsymbol{q}(r, z, \omega)$ is sought in the higher-dimensional space $\Omega_p \times \Omega_\omega$. The PGD methodology [33–35, 43, 50] can be succinctly summarised in three steps:

1. $\boldsymbol{q}(r,z,\omega)$ is assumed to be approximable by a separable function $\boldsymbol{q}^N(r,z,\omega)$ defined as in [39] with one parametric mode for every component

$$\boldsymbol{q}(r,z,\omega) \approx \boldsymbol{q}^N(r,z,\omega) = \sum_{n=1}^{N} \boldsymbol{\beta}^n \odot \boldsymbol{F}^n(r,z) G^n(\omega), \tag{25}$$

where each n^{th} term of the above series is the product of normalised separable functions $\boldsymbol{F}^n(r,z) \in X(0) \times Y(\mathbf{0})$ and $G^n(\omega) \in Z = L^2(\Omega_\omega)$ and a weight vector $\boldsymbol{\beta}^n$, with $\odot$ representing the element-wise Hadamard product as defined in [51]. Note that the non-homogeneous Dirichlet boundary conditions are incorporated within the first mode.

2. Each term n is sequentially obtained using a Greedy algorithm [50].

3. For a given term n, functions $\boldsymbol{F}^n(r,z)$ and $G^n(\omega)$ are computed iteratively with an alternating directions fixed-point algorithm [33].

In general, for a given n^{th} term of above series (25), the accumulated solution $\boldsymbol{q}^n(r,z,\omega)$ can be written as

$$\boldsymbol{q}^n(r,z,\omega) = \boldsymbol{q}^{n-1}(r,z,\omega) + \boldsymbol{f}(r,z) g(\omega) \qquad\qquad n = 1, 2 \cdots N, \tag{26}$$

where $\boldsymbol{f}(r,z)g(\omega)$ denotes an approximation which is assumed to converge to $\boldsymbol{\beta}^n \odot \boldsymbol{F}^n(r,z) G^n(\omega)$ through the alternating directions fixed-point algorithm, with $\boldsymbol{f}(r,z) \in X(0) \times Y(\mathbf{0})$ and $g(\omega) \in Z$. In this work, we have adopted the following representation for the weight vector $\boldsymbol{\beta}^n = \begin{bmatrix} \beta^n_{\mathcal{A}_\phi} & \beta^n_{\boldsymbol{u}} & \beta^n_{\overline{\boldsymbol{u}}} \end{bmatrix}^T$, with $||\boldsymbol{F}^n||_{L^2(\Omega_\omega)} = 1$ and $||G^n||_{L^2(\Omega_\omega)} = 1$. A suitable (compatible) test (or virtual) field to $\boldsymbol{f}(r,z)g(\omega)$ can then be introduced as

$$\delta\boldsymbol{q}(r,z,\omega) = \delta\boldsymbol{f}(r,z) g(\omega) + \boldsymbol{f}(r,z) \delta g(\omega), \tag{27}$$

with $\delta\boldsymbol{f}(r,z) \in X(0) \times Y(\mathbf{0})$ and $\delta g(\omega) \in Z$. In this case, substitution of (26) and (27) into the augmented weak form (20), permits the alternating directions fixed-point algorithm for the computation of the n^{th} term in (25) to be formulated as: Find $(\boldsymbol{f}, g) \in X(0) \times Y(\mathbf{0}) \times Z$ such that

$$\mathcal{R}_f(\delta\boldsymbol{f}; \boldsymbol{q}^{n-1}, \boldsymbol{f}, g) + \mathcal{R}_g(\delta g; \boldsymbol{q}^{n-1}, \boldsymbol{f}, g) = 0 \qquad \forall (\delta\boldsymbol{f}, \delta g) \in X(0) \times Y(0) \times Z, \tag{28}$$

with

$$\begin{aligned} \mathcal{R}_f(\delta\boldsymbol{f}; \boldsymbol{q}^{n-1}, \boldsymbol{f}, g) :=\ & G_0(g,g) W_K(\boldsymbol{f}, \delta\boldsymbol{f}) + \mathrm{i} G_1(g,g) W_C(\boldsymbol{f}, \delta\boldsymbol{f}) \\ & - G_2(g,g) W_M(\boldsymbol{f}, \delta\boldsymbol{f}) - G_0(1,g) S(\delta\boldsymbol{f}) \\ & + \mathcal{W}_K(\boldsymbol{q}^{n-1}, g\delta\boldsymbol{f}) + \mathrm{i}\mathcal{W}_C(\boldsymbol{q}^{n-1}, g\delta\boldsymbol{f}) - \mathcal{W}_M(\boldsymbol{q}^{n-1}, g\delta\boldsymbol{f}), \end{aligned} \tag{29a}$$

$$\begin{aligned} \mathcal{R}_g(\delta g; \boldsymbol{q}^{n-1}, \boldsymbol{f}, g) :=\ & G_0(g,\delta g) W_K(\boldsymbol{f}, \boldsymbol{f}) + \mathrm{i} G_1(g,\delta g) W_C(\boldsymbol{f}, \boldsymbol{f}) \\ & - G_2(g,\delta g) W_M(\boldsymbol{f}, \boldsymbol{f}) - G_0(1,\delta g) S(\boldsymbol{f}) \\ & + \mathcal{W}_K(\boldsymbol{q}^{n-1}, \boldsymbol{f}\delta g) + \mathrm{i}\mathcal{W}_C(\boldsymbol{q}^{n-1}, \boldsymbol{f}\delta g) - \mathcal{W}_M(\boldsymbol{q}^{n-1}, \boldsymbol{f}\delta g), \end{aligned} \tag{29b}$$

where

$$G_0(a,b) := \int_{\Omega_\omega} a\bar{b}\,\mathrm{d}\omega, \quad G_1(a,b) := \int_{\Omega_\omega} a\bar{b}\omega\,\mathrm{d}\omega, \quad G_2(a,b) := \int_{\Omega_\omega} a\bar{b}\omega^2\,\mathrm{d}\omega. \tag{30}$$

4.1 Solve for $\boldsymbol{f}$ and g using the Alternating Direction Scheme (ADS) method

In order to solve (28), the $[k]$-iterative ADS method is typically preferred [33]; first solving for $\boldsymbol{f}^{[k+1]}$ based on a known value of $g^{[k]}$ and then updating $g^{[k+1]}$ with the newly computed $\boldsymbol{f}^{[k+1]}$. The ADS method can be summarised as: Find $(\boldsymbol{f}^{[k+1]}, g^{[k+1]}) \in X(0) \times Y(\mathbf{0}) \times Z$ such that

$$\mathcal{R}_{\boldsymbol{f}}(\delta\boldsymbol{f}; \boldsymbol{q}^{n-1}, \boldsymbol{f}^{[k+1]}, g^{[k]}) = 0, \quad \mathcal{R}_g(\delta g; \boldsymbol{q}^{n-1}, \boldsymbol{f}^{[k+1]}, g^{[k+1]}) = 0, \tag{31}$$

for all $(\delta\boldsymbol{f}, \delta g) \in X(0) \times Y(0) \times Z$, where $[k] = 1, 2, \ldots$ denotes the fixed-point iteration and the stopping criteria is presented in Section 4.3. Alternatively, the solution fields $\boldsymbol{f}^{[k+1]}$ and $g^{[k+1]}$ can be written as

$$\boldsymbol{f}^{[k+1]} = \boldsymbol{f}^{[k]} + \Delta\boldsymbol{f}, \quad g^{[k+1]} = g^{[k]} + \Delta g, \tag{32}$$

and thus, (31) can be re-written by making use of the concept of directional derivatives [52] as: Find $(\Delta\boldsymbol{f}, \Delta g) \in X(0) \times Y(\mathbf{0}) \times Z$ such that

$$D\mathcal{R}_{\boldsymbol{f}}(\delta\boldsymbol{f}; \boldsymbol{f}^{[k]}, g^{[k]})[\Delta\boldsymbol{f}] = -\mathcal{R}_{\boldsymbol{f}}(\delta\boldsymbol{f}; \boldsymbol{q}^{n-1}, \boldsymbol{f}^{[k]}, g^{[k]}), \tag{33a}$$

$$D\mathcal{R}_g(\delta g; \boldsymbol{f}^{[k+1]}, g^{[k]})[\Delta g] = -\mathcal{R}_g(\delta g; \boldsymbol{q}^{n-1}, \boldsymbol{f}^{[k+1]}, g^{[k]}), \tag{33b}$$

for all $(\delta\boldsymbol{f}, \delta g) \in X(0) \times Y(\mathbf{0}) \times Z$. Above residual equations (33) can be sequentially solved for $\Delta\boldsymbol{f}$ and Δg in order to iteratively evolve the ADS algorithm as shown in (32). The directional derivatives appearing in (33) can be expanded as

$$\begin{aligned} D\mathcal{R}_{\boldsymbol{f}}(\delta\boldsymbol{f}; \boldsymbol{f}, g)[\Delta\boldsymbol{f}] &= G_0(g,g)W_K(\Delta\boldsymbol{f}, \delta\boldsymbol{f}) + G_1(g,g)W_C(\Delta\boldsymbol{f}, \delta\boldsymbol{f}) \\ &\quad - M_2(g,g)W_M(\Delta\boldsymbol{f}, \delta\boldsymbol{f}), \end{aligned} \tag{34a}$$

$$\begin{aligned} D\mathcal{R}_g(\delta g; \boldsymbol{f}, g)[\Delta g] &= W_K(\boldsymbol{f}, \boldsymbol{f})G_0(\Delta g, \delta g) + W_C(\boldsymbol{f}, \boldsymbol{f})G_1(\Delta g, \delta g) \\ &\quad - W_M(\boldsymbol{f}, \boldsymbol{f})G_2(\Delta g, \delta g), \end{aligned} \tag{34b}$$

and the residuals have been already defined in (29).

4.2 Discretised system

This Section briefly presents the discretised problem (33) using the standard Bubnov-Galerkin approximation. The finite element computational domain will be discretised generating an unstructured triangular mesh, defining a non-overlapping partition $(\mathcal{V}, \mathcal{E}, \mathcal{I})$, where $\mathcal{V}$ denotes the set of vertices, $\mathcal{E}$ the set of edges and $\mathcal{I}$ the set of cells. In each element, the H^1 conforming hierarchic finite element basis functions [53] are employed. Hence, the spatial discretisation of the fields $\mathcal{A}_\phi$ and $\boldsymbol{u}$ allows an arbitrary increase in element order p

and local refinement of the mesh spacing h. The discretised system is obtained by replacing the fields $\Delta\boldsymbol{f}$, $\delta\boldsymbol{f}$, Δg and δg in (33) by the discrete variables as

$$\begin{aligned} \Delta\boldsymbol{f} &= \sum_{a=1}^{P} N_a \Delta\mathbf{f}_a, \quad \delta\boldsymbol{f} = \sum_{b=1}^{P} N_b \delta\mathbf{f}_b, \\ \Delta g &= \sum_{a=1}^{Q} N_a \Delta\mathrm{g}_a, \quad \delta g = \sum_{b=1}^{Q} N_b \delta\mathrm{g}_b, \end{aligned} \tag{35a}$$

where N_a is a typical shape function and $P = P_{\mathcal{V}} + P_{\mathcal{E}} + P_{\mathcal{I}}$ and $Q = Q_{\mathcal{V}} + Q_{\mathcal{E}} + Q_{\mathcal{I}}$ are the number of degrees of freedom of the spatial and frequency problems, respectively. The global system is constructed from the elemental matrices and vectors by a standard assembly procedure [15]. Thus, the global discrete expression of the spatial problem (33a) is

$$(g_0\mathbf{K} + \mathrm{i}g_1\mathbf{C} - g_2\mathbf{M})\Delta\mathbf{f} = -\mathbf{R}_{\boldsymbol{f}}(\boldsymbol{f}^{[k]}, g^{[k]}). \tag{36}$$

Note that here and in the following we use Roman boldface to describe discrete matrix/vector quantities. The discretised version of the residual is defined as

$$\mathbf{R}_{\boldsymbol{f}}(\boldsymbol{f}, g) = (g_0\mathbf{K} + \mathrm{i}g_1\mathbf{C} - g_2\mathbf{M})\mathbf{f} - g_0^s\mathbf{s} + \sum_{m=1}^{n-1}\Big[g_0^{[m]}\mathbf{K} + \mathrm{i}g_1^{[m]}\mathbf{C} - g_2^{[m]}\mathbf{M}\Big]\mathbf{F}^{[m]}, \tag{37}$$

with the following scalar quantities

$$\begin{aligned} g_0 &= G_0(g, g), & g_0^{[m]} &= G_0(G^{[m]}, g), \\ g_1 &= G_1(g, g), & g_1^{[m]} &= G_1(G^{[m]}, g), \\ g_2 &= G_2(g, g), & g_2^{[m]} &= G_2(G^{[m]}, g). \\ g_0^s &= G_0(1, g), \end{aligned} \tag{38}$$

Similarly, the problem on the frequency domain (33b) can be written in its discrete from as

$$(k\mathbf{G}_0 + \mathrm{i}c\mathbf{G}_1 - m\mathbf{G}_2)\Delta\mathbf{g} = -\mathbf{R}_g(\boldsymbol{f}^{[k+1]}, g^{[k]}), \tag{39}$$

where the residual is defined as

$$\mathbf{R}_g(\boldsymbol{f}, g) = (k\mathbf{G}_0 + \mathrm{i}c\mathbf{G}_1 - m\mathbf{G}_2)\mathbf{g} - s\mathbf{g}_1 + \sum_{m=1}^{n-1}\Big[k^{[m]}\mathbf{G}_0 + \mathrm{i}c^{[m]}\mathbf{G}_1 - m^{[m]}\mathbf{G}_2\Big]\mathbf{G}^{[m]}, \tag{40}$$

with the following scalar quantities

$$\begin{aligned} k &= W_K(\boldsymbol{f}, \boldsymbol{f}), & k^{[m]} &= W_K(\boldsymbol{F}^{[m]}, \boldsymbol{f}), \\ c &= W_C(\boldsymbol{f}, \boldsymbol{f}), & c^{[m]} &= W_C(\boldsymbol{F}^{[m]}, \boldsymbol{f}), \\ m &= W_M(\boldsymbol{f}, \boldsymbol{f}), & m^{[m]} &= W_M(\boldsymbol{F}^{[m]}, \boldsymbol{f}). \\ s &= S(\boldsymbol{f}), \end{aligned} \tag{41}$$

In this paper, it will prove useful to use an alternative Petrov-Galerkin methodology when solving (33b), where the test function δg associated to a frequency ω_a is chosen to be the Dirac delta distribution defined as $\delta g = \delta(\omega - \omega_a)$ and, thus, the discretised system becomes

$$(k\mathbf{I} + \mathrm{i}c\boldsymbol{\omega} - m\boldsymbol{\omega}^2)\Delta\mathbf{g} = -\mathbf{R}_g(\boldsymbol{f}^{[k+1]}, g^{[k]}), \tag{42}$$

where the residual is defined as

$$\mathbf{R}_g(\boldsymbol{f}, g) = (k\mathbf{I} + \mathrm{i}c\boldsymbol{\omega} - m\boldsymbol{\omega}^2)\mathbf{g} - s\mathbf{1} + \sum_{m=1}^{n-1}\left[k^{[m]}\mathbf{I} + \mathrm{i}c^{[m]}\boldsymbol{\omega} - m^{[m]}\boldsymbol{\omega}^2\right]\mathbf{G}^{[m]}, \tag{43}$$

with $\mathbf{I}$ is the identity matrix of dimension the size of the parametric domain N_ω, $\mathbf{1}$ is a vector of ones of dimension N_ω and $\boldsymbol{\omega} = \mathrm{diag}(\omega_1, \cdots, \omega_{N_\omega})$.

4.3 Stopping criteria

The PGD methodology involves two iterative procedures which require appropriate stopping criteria; one required to control the convergence of the ADS fixed point algorithm (31) and another one needed to control the so-called Greedy algorithm (26), namely, the number of PGD modes required to achieve a reasonably accurate solution. For the ADS convergence, our preferred measure of tolerance is defined through the following error norm

$$e_{FP} = \frac{||\boldsymbol{f}^{[k+1]}g^{[k+1]} - \boldsymbol{f}^{[k]}g^{[k]}||_{L^2(\Omega_p\times\Omega_\omega)}}{||\boldsymbol{f}^{[k+1]}g^{[k+1]}||_{L^2(\Omega_p\times\Omega_\omega)}} \leq tol_{FP}, \tag{44}$$

where tol_{FP} is a user-defined tolerance value. Whenever the criterion (44) is satisfied, the PGD algorithm advances to the next enrichment step (or mode). To monitor and control the number of modes added to the series (25), the following two error norms are monitored

$$e^n_{EM,N} = \frac{\beta^n_{\mathcal{A}_\phi}}{\sum_{m=1}^{n}\beta^{[m]}_{\mathcal{A}_\phi}} \leq tol_N, \qquad e^n_{M,N} = \frac{\beta^n_{\boldsymbol{u}}}{\sum_{m=1}^{n}\beta^{[m]}_{\boldsymbol{u}}} \leq tol_N, \tag{45}$$

where tol_N is another user-defined tolerance value and above criteria (45) permit control independently the convergence of the vector potential and the displacement field vectors of the PGD approximation.

4.4 Algorithmic flowchart of the PGD algorithm

In this Section, two algorithmic flowcharts, corresponding to the offline and online stages, of the PGD methodology are presented. Firstly, Figure 5 shows the workflow of the offline PGD stage described in Section 4. Secondly, Figure 6 displays the interpolation proce-

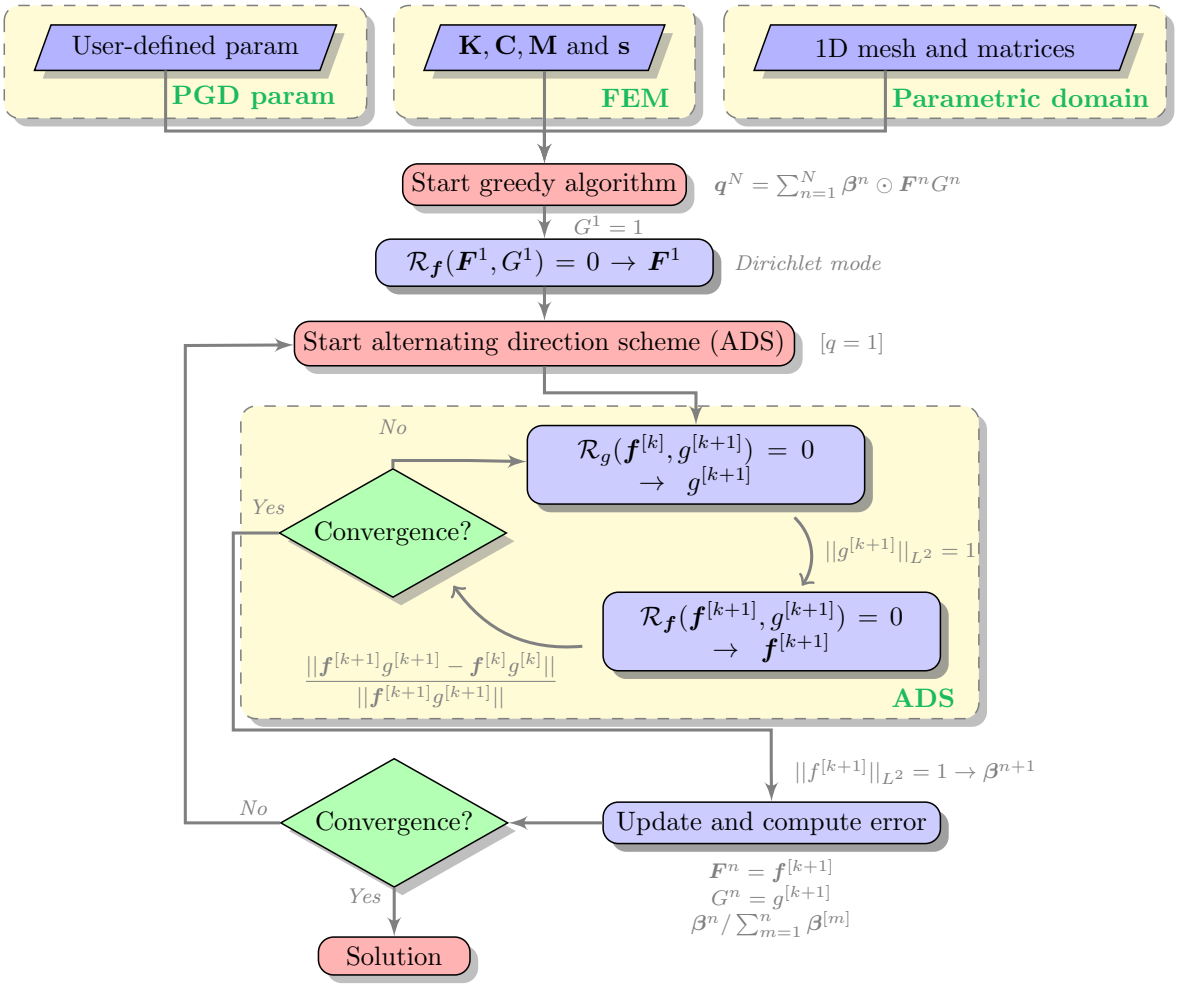

Figure 5: Flow chart of PGD algorithm; description of the offline stage.

dure to compute the parametric solution for the desired (user-defined) set of parameters $(\mathbf{r}, \mathbf{z}, \boldsymbol{\omega})$,[3] being thus able to achieve so-called *real-time* simulations [41].

5 Regularised-adaptive PGD methodology

Numerical singularities in the vicinity of the conductors' resonant modes can arise when simulating the coupled magneto-mechanical problem. In order to motivate the numerical difficulties encountered and introduce our regularised-adaptive PGD methodology, a simplified coupled magneto-mechanical MRI test problem consisting is set up, consisting of a conducting mechanical shell Ω_p^C located within a non-conducting domain, as presented in

[3]Bold non-italisiced fonts $(\mathbf{r}, \mathbf{z}, \boldsymbol{\omega})$ are used to symbolise the discrete set of user-defined parameters in the multiple-query stage.

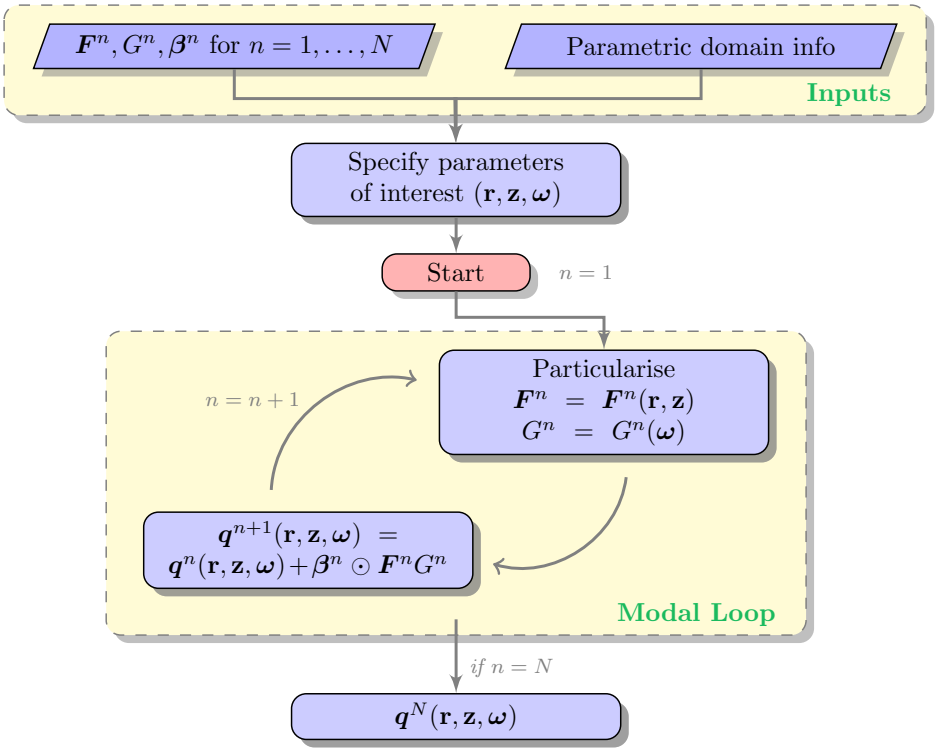

Figure 6: Flow chart of PGD algorithm; description of the online stage.

Figure 7a. The problem is excited through a pressure driven force applied on the conducting shell.

In the context of an MRI problem, two main integrated quantities of interest are typically analysed, namely, the dissipated or Ohmic power and the kinetic energy, which can be computed as a postprocess of the solution fields as[4]

$$P^0_{\Omega^C} = \frac{1}{2}\int_{\Omega^C} \gamma |\boldsymbol{\mathcal{E}}^{AC}|^2 \mathrm{d}\Omega, \qquad E^k_{\Omega^C} = \frac{1}{2}\int_{\Omega^C} \rho\omega^2 |\boldsymbol{\mathcal{U}}^{AC}|^2 \mathrm{d}\Omega. \tag{46}$$

By sweeping over frequencies along the range of interest, the response of the MRI scanner (conducting shell) for these quantities of interest can be obtained. This frequency spectrum is presented in Figure 7b, where the resonance modes are clearly visible in the form of singularities. These sharp changes in the kinetic energy can make extremely challenging the convergence of the PGD algorithm due to the ill-conditioning of the resulting PGD system in the proximity of these resonance modes. As a result, two main strategies have been devised in order to overcome these numerical difficulties; first, the addition of numerical regularisation and, second, an automatic adaptive PGD splitting of the frequency interval.

[4]The integrated quantities in (46) have been presented in its three-dimensional form. The reader is referred to [20] for the axisymmetric description of these quantities.

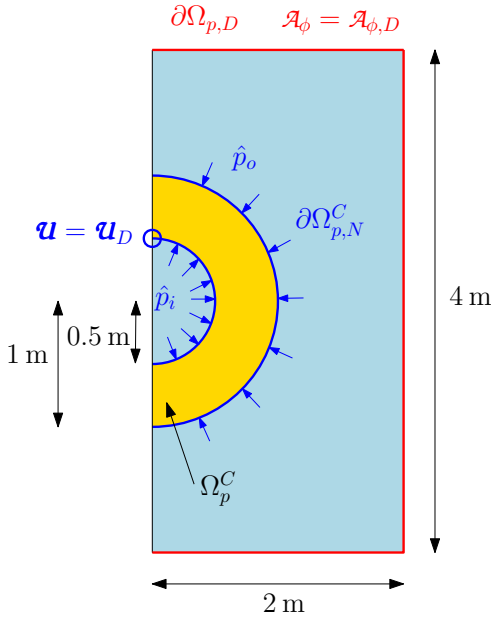

(a) Geometry and boundary conditions description.

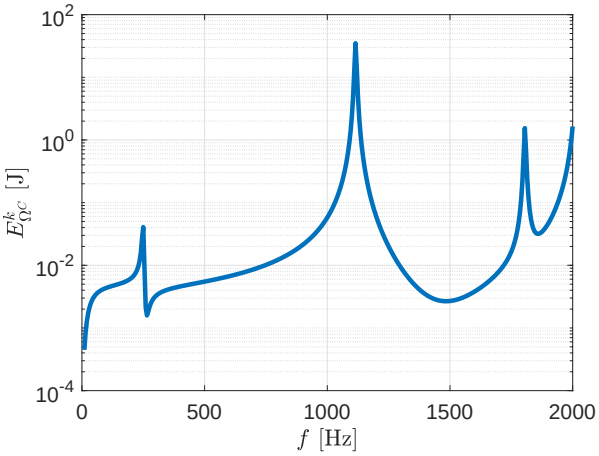

(b) Kinetic energy $E^k_{\Omega^C}$ in the conducting mechanical shell. Mesh of 351 triangular elements with polynomial order $p = 3$.

Figure 7: Magneto-mechanical test problem; geometry description and kinetic energy in the conducting mechanical shell.

5.1 Numerical regularisation

Numerical regularisation is simply introduced in our algorithm through the addition of mechanical damping which, in its simplest form, can be formulated as Rayleigh mass based damping [15], where a damping contribution proportional to the mass of the system is considered, as presented in [16], with α the Rayleigh damping coefficient used to adjust the level of regularisation added into the system.

In Figure 8, the kinetic energy in the conducting mechanical shell Ω^C_p is plotted for different values of the damping parameter α. The mesh used for these simulations consists of 351 triangular elements with polynomial order $p = 3$, which produces a fully resolved full order solution. It is interesting to observe that the resonant frequencies remain unaffected regardless of the damping introduced but with lower energetic contributions. This shows how the use of numerical regularisation helps reduce the ill-conditioning of the overall system near resonant modes, without modifying the overall energy spectrum [15]. This is confirmed in Figure 8, where the singularities at resonant frequencies are dramatically reduced.

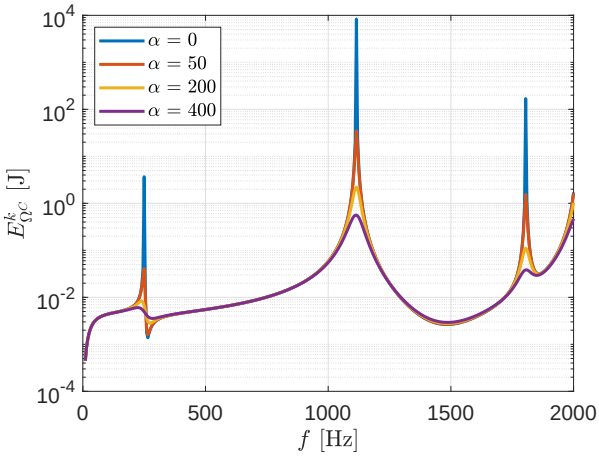

Figure 8: Magneto-mechanical test problem; values of the kinetic energy $E^k_{\Omega^C}$ in the mechanical shell Ω^C_p for different damping parameters α.

5.2 Automatic adaptive PGD splitting

The resonant phenomenon has been illustrated in Figure 7b and stated how this can negatively affect the solution of the PGD algorithm. Indeed, if the workflow as described in Section 4.4 was to be applied directly, it would not immediately yield an accurate approximation of the solution. This can be observed in Figure 9a, where the PGD solution (in green) is compared against the full order solution (in blue), the latter used as the benchmark for comparison. Noticeable differences between both graphs can be easily appreciated. Nonetheless, we can still use this PGD first approximation in order to approximately identify the location of the largest (in response) resonant mode in an automatic manner, meaning that the *a priori* nature of the PGD methodology (no beforehand knowledge of the solution required) is preserved.

Once a singularity (or several singularities) has (have) been identified, partitioned frequency subdomains (clusters) can be defined and a refined PGD solution is computed within these subdomains, that can better capture the overall solution, see Figure 9b. This three-step process of *i*) identification of resonance modes (in green), *ii*) frequency interval splitting and *iii*) adaptive PGD calculation (in orange), might need to be repeated several times until convergence is achieved, namely, after no further resonance frequencies are detected. For the example considered here, the process was repeated three times before converging to the final PGD approximation displayed in Figure 9d. As can be observed, differences between the full and the PGD solutions are virtually undistinguishable. Notice that the splitting in step *ii*) is carried out by setting a tolerance value tol^{ω}_{split} that controls the size of the subdomains, obtaining frequency subdomains that are neither too small nor too large. Once the singularities are approximately identified (in green), the refined PGD solution (in orange) is used to accurately approximate the full order model.

For this problem, the user-defined parameters are shown in Table 1. I_N and I_{FP}

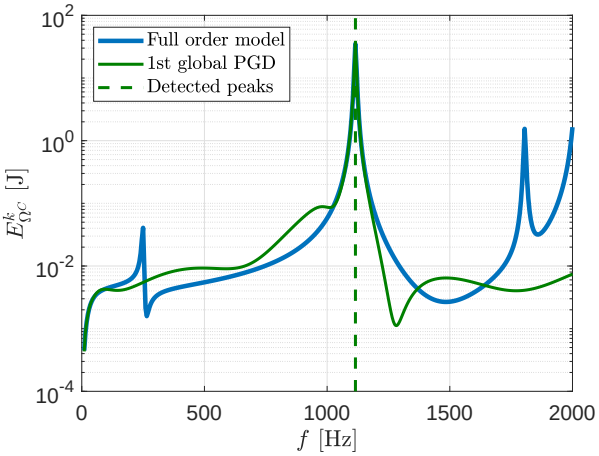

(a) 1^{st} step; global PGD over the entire interval of interest. Low accuracy of the approximation but good identification of some singularities.

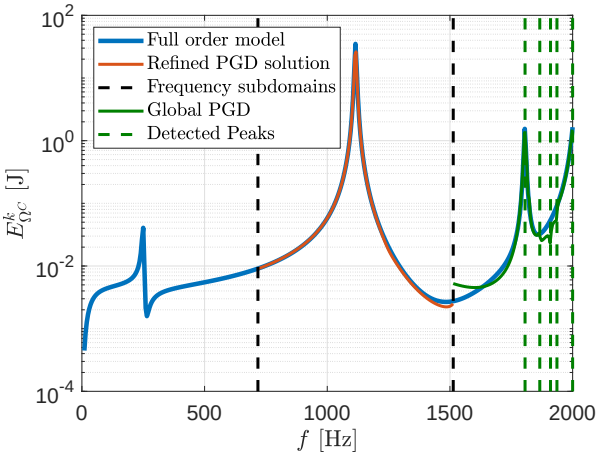

(b) 2^{nd} step; refined PGD solution around resonant frequencies and global PGD to next domain (repeat until all subdomains have a refined PGD solution).

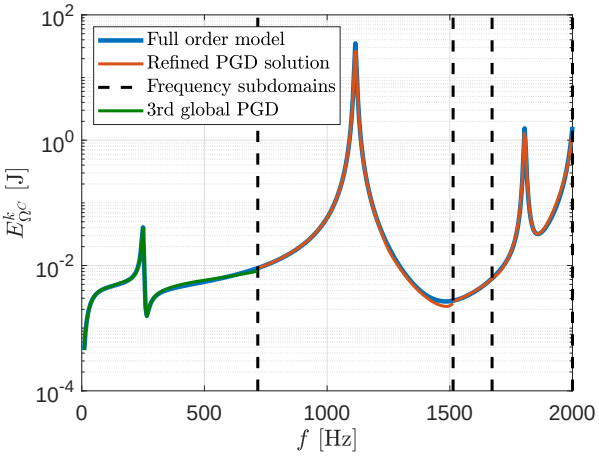

(c) 3^{rd} step; refined PGD solution around resonant frequencies and global PGD to next domain (repeat until all subdomains have a refined PGD solution).

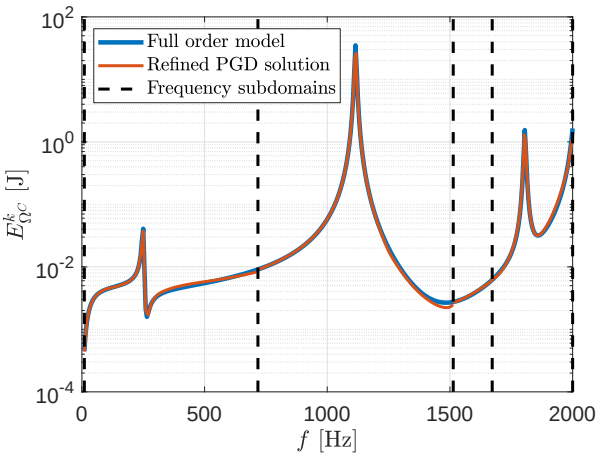

(d) 4^{th} step; solution of the regularised-adaptive PGD.

Figure 9: Magneto-mechanical test problem; description of the automatic splitting process performed to locate the resonance frequencies and refine around them. Plot of kinetic energy $E^k_{\Omega^C}$ in the conducting mechanical shell with a damping coefficient $\alpha = 50$.

denote the maximum number of PGD modes and fixed-point iterations, respectively; tol_N and tol_{FP} are the tolerance values used for the stopping criteria of the greedy and ADS algorithms, respectively, as defined in (45) and (44). As for the spatial domain Ω_p, its discretisation is defined by the mesh size h, the number of triangular elements $E_{\Omega_p^C}$ and the polynomial order p. In addition, α denotes the damping coefficient. As for the parametric domain Ω_ω, the mesh size is h_ω, the frequency range is defined by the interval range

Table 1: User-defined parameters for the simulation in Figure 9.

Global PGD parameters				Refined PGD parameters			
I_N	I_{FP}	tol_N	tol_{FP}	I_N	I_{FP}	tol_N	tol_{FP}
10	5	10^{-4}	10^{-2}	20	10	10^{-4}	10^{-2}
Spatial domain Ω_p				Parametric domain Ω_ω			
h	$E_{\Omega_p^C}$	p	α	h_ω	ω_{min}	ω_{max}	tol^ω_{split}
0.25	351	3	50	0.01	1 Hz	2000 Hz	0.02

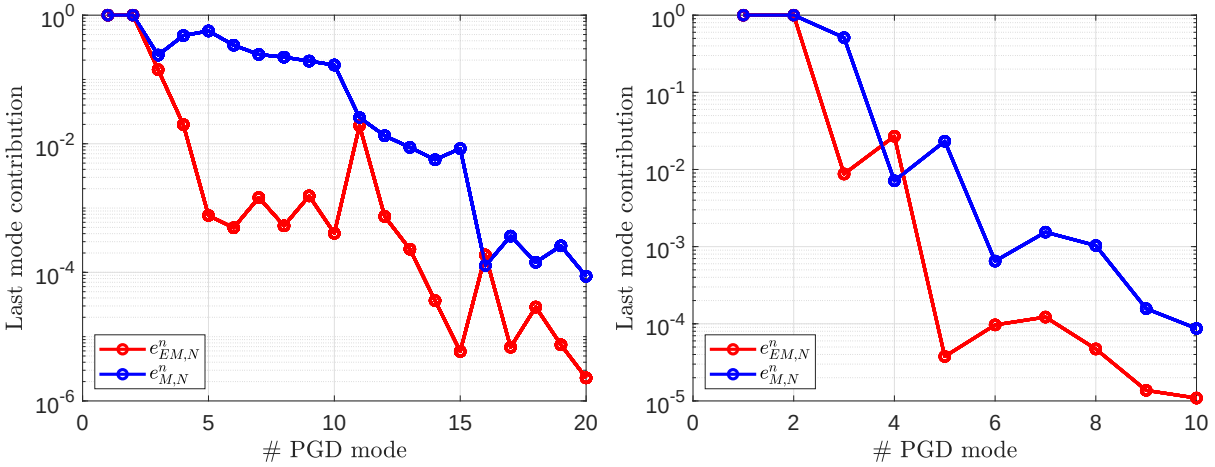

(a) 1^{st} frequency subdomain: [10, 717] Hz. (b) 2^{nd} frequency subdomain: [717, 1513] Hz.

Figure 10: Magneto-mechanical test problem; PGD convergence using the last mode contribution for both physics; electromagnetics $e^n_{EM,N}$ and mechanics $e^n_{M,N}$.

$[\omega_{min}, \omega_{max}]$ and the tolerance when splitting the frequency domain is denoted by tol^ω_{split}, which controls the maximum size of the resulting subdomains. Note that the parameters I_N, I_{FP} used for the refined PGD solution are larger than those used for the less accurate global PGD solution (employed for the localisation of resonant modes). The reduction in ADS iterations and the coarsening of the computational frequency interval implies less computational cost without sacrificing numerical accuracy.

As for the greedy algorithm, modal contributions for both physics, namely, electromagnetics $e^n_{EM,N}$ and mechanics $e^n_{M,N}$ (45), are computed and plotted in Figure 10 for the first two frequency subdomains [10, 717] and [717, 1513] Hz. There is a clear overall descending trend in both subdomains yet with some modes having a higher weight than their predecessors, which is one of the characteristics of the greedy algorithm [34].

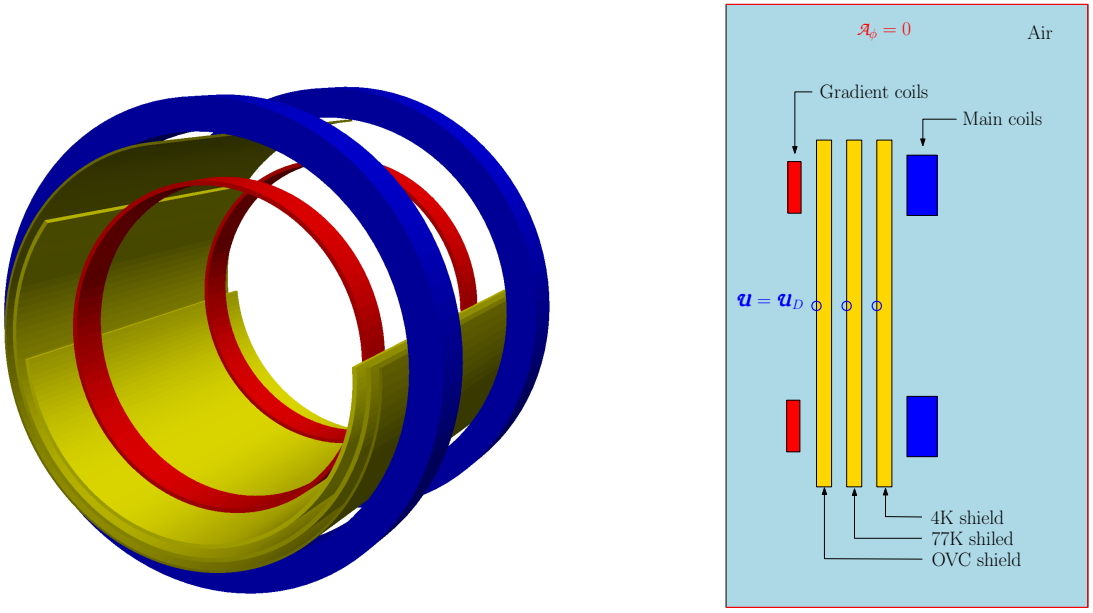

Figure 11: Test magnet problem; geometry description. 3D view (left) and 2D axisymmetric view (right) with components names and boundary conditions.

6 Numerical examples

This section includes a series of numerical examples in order to demonstrate the validity, applicability and versatility of the proposed PGD methodology. Two different MRI magnet configurations will be studied. First, a simplified tailor-made MRI (test) magnet problem followed by a realistic, and more challenging, MRI configuration. In both cases, the PGD approximation will first be validated against the full order model. The presence of numerical difficulties such as the existence of resonant modes will be circumvented through the adaptive-regularised strategy presented in the previous section. It will shown how the combination of both frequency domain adaptive splitting and the use of numerical regularisation in the vicinity of resonant modes, leads to a robust and versatile PGD algorithm. A comprehensive set of results will be shown with special emphasis on magnitudes of interest for the industry (46). The section will conclude by presenting snapshots of our PGD online tablet tool demonstrating the flexibility of the new methodology for fast prototyping.

6.1 Test magnet problem

The test magnet problem corresponds to a simplified MRI scanner geometry, which consists of three conducting shields embedded in a non conducting rectangular domain, see Figure 11. The three shields are known as the Outer Vacuum Chamber (OVC) shield Ω^C_{OVC}, the 77K radiation shield Ω^C_{77K} and the 4K helium vessel shield Ω^C_{4K} and they have different material parameters that cannot be exactly specified due to confidentiality issues. However,

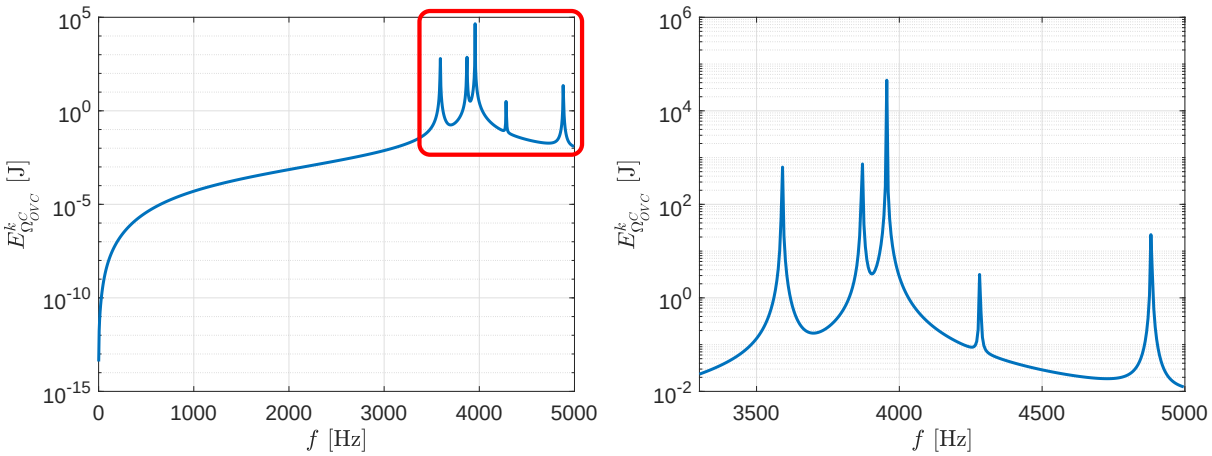

Figure 12: Test magnet problem; value of the dissipated Power $E^k_{\Omega^C_{OVC}}$ in the OVC shield for different frequencies from 1 to 5000 Hz. Right Figure shows a zoomed view in the resonance region (red rectangle). Results shown are for a mesh of 2.9K triangular elements using a polynomial order $p = 4$.

the approximate values are $\mu_* \approx 10^{-7}$ H/m, $\gamma_* \approx 10^6$ S/m, $\rho \approx 10^3$ Kg/m^3, $E \approx 10^9$ Pa, $\nu \approx 0.3$. The thickness of each shield is slightly different and it is of the order of a few millimetres. The problem is excited through the current sources $\boldsymbol{J}^{DC}$ and $\boldsymbol{\jmath}^{AC}$ that create a uniform magnetic field of strength $B_0 = \max(||\boldsymbol{B}_0^{DC}|_{r=0}||) = 1.5$ T and a gradient along the $r = 0$ axis of $||\partial \boldsymbol{\mathcal{B}}_0^{AC}|_{r=0}/\partial z|| = 100$ mT/m, respectively. Regarding the boundary conditions, displacements $\boldsymbol{u} = \boldsymbol{u}_D = \boldsymbol{0}$ are fixed to a small part in the centre of each shield and the scalar potential is set to $\mathcal{A}_\phi = \mathcal{A}_{\phi,D} = 0$ far away from the conducting objects such that $\boldsymbol{n} \times \boldsymbol{\mathcal{A}}^{AC} = \boldsymbol{0}$ on $\partial\Omega$.

6.1.1 Full order model

The frequency range of interest is set from 1 to 5000 Hz and Figure 12 shows the values of the kinetic energy $E^k_{\Omega^C_{OVC}}$ in this frequency range. The results show a smooth trend up to 3500 Hz followed by resonance when approaching the high-frequency range, from 3500 to 5000 Hz. The accurate identification of this phenomenon is of extreme interest for the design of the MRI scanner, as high eddy currents can generate large displacements which can, in turn, lead to excessive heat radiation within the helium vessel. The helium contained within the vessel is at 4 K and exceeding this value can result in an undesired boil-off effect, requiring then the re-fill of the vessel which increases the maintenance costs. Another consequence of the existence of resonance is that high vibrations of the mechanical components can have a negative impact on the lifespan of the MRI.

In Figure 13 a convergence analysis is presented in order to demonstrate the consistency of the numerical scheme employed in the solution of the full order model [20, 21, 24]. This analysis is important prior to developing a PGD approximation to the full order method,

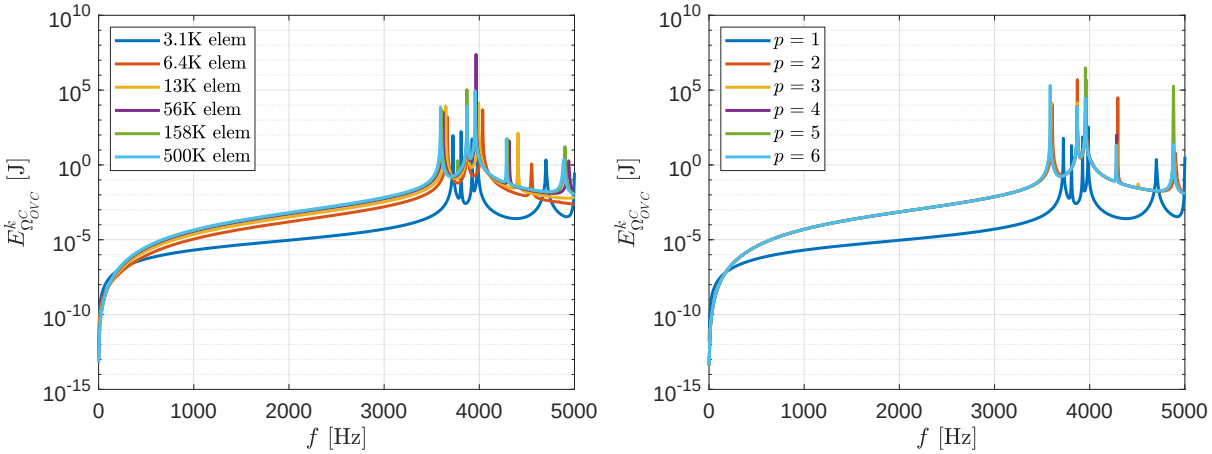

Figure 13: Test magnet problem; h-refinement (left) using a polynomial order $p = 1$ and p-refinement (right) with a mesh of 2.9K elements.

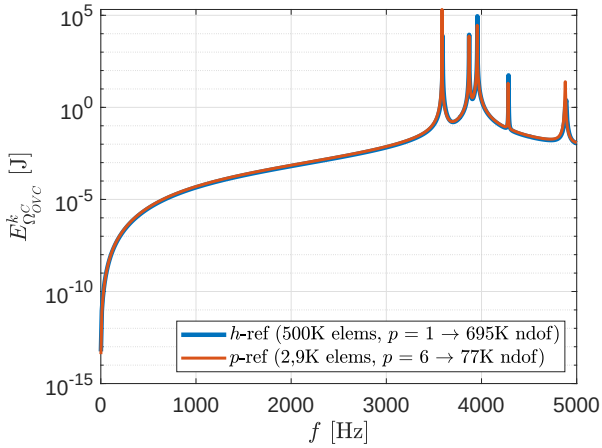

Figure 14: Test magnet problem; comparison between solutions obtained with a mesh with 500K elements with $p = 1$ and a mesh with $p = 6$ with 2.9K elements.

so that h- and p-refinement studies are carried out and results displayed in Figure 13. Comparison of Figures 13 (left) and (right), demonstrates that p-refinement leads more efficiently to a converged solution. Figure 14 shows the converged solution obtained with either refinement strategies which agree well. However, whilst the 500K element mesh and $p = 1$ results in 695K degrees of freedom (ndof), only 77K ndof are used in 2.9K element mesh and $p = 6$. In this case, the results suggest that increasing the polynomial order p is a good strategy to accurately capture the skin depth effect inside the thin conducting shields without the need to resort to a prohibitively large number of degrees of freedom.

A further study explores the number of sampling points required in order to obtain an accurate energy spectrum. Figures 12, 13 and 14 have been obtained sweeping over the frequency range with sampling points every 5 Hz. In order to certify that a 5 Hz spacing is

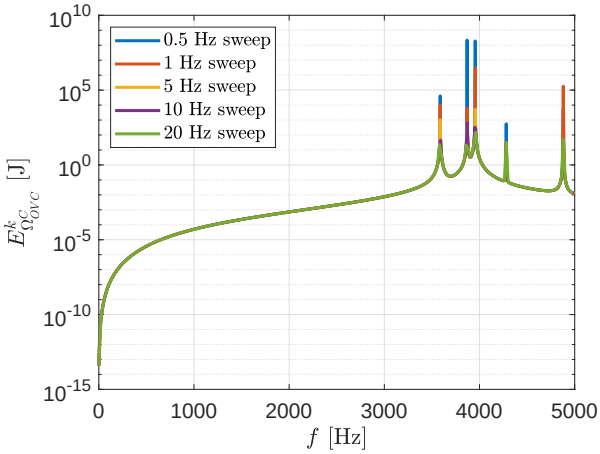

Figure 15: Test magnet problem; study on the number sampling of points in the frequency interval required to accurately capture the solution.

sufficient, Figure 15 is presented, where frequency energy spectra for five different frequency spacings are displayed, namely, every 0.5, 1, 5, 10 and 20 Hz. The main conclusion than can be extracted from these results is that a 5 Hz spacing is sufficient to accurately represent the spectrum and capture the resonance modes. Notice that this is only applicable to this specific problem and it should not be generalised to other MRI configurations.

Figure 16 shows the magnitude of the transient magnetic field $|\boldsymbol{\mathcal{B}}_0^{AC}|$ in the axisymmetric plane in the form of contour lines, where the magnitude of the displacement field $|\boldsymbol{\mathcal{U}}|$ is also plotted in the OVC shield as well as the deformed shape of the shield. The six subfigures correspond to six different frequencies, one at the pre-resonant frequency of 2000 Hz and the other five at the resonance frequencies obtained from Figure 12, namely, 3591, 3871, 3956, 4281 and 4881 Hz. Regarding the magnetic field $|\boldsymbol{\mathcal{B}}_0^{AC}|$, major changes are not visible when increasing the excitation frequency, yet it is interesting to notice how this magnetic field is generated in the gradient coils and travels through the free space permeating across the conducting shields.

On the other hand, major changes can be seen in the magnitude of the displacement field $|\boldsymbol{\mathcal{U}}|$. Figure 16a represents the displacement that would be typically observed for frequencies in the pre-resonance region, where the maximum values are concentrated in regions near the gradient coils that generate the transient magnetic field. Figures 16b-16f, display the displacement fields for the first resonant modes of the spectrum.

6.1.2 PGD solution

Section 5 described our methodology to circumvent the numerical difficulties arising from the ill-conditioning of the PGD system by combining an automatic frequency domain splitting and numerical regularisation. This section aims to benchmark the PGD approximation against the full order model by comparing two quantities of interest, namely, dissipated or

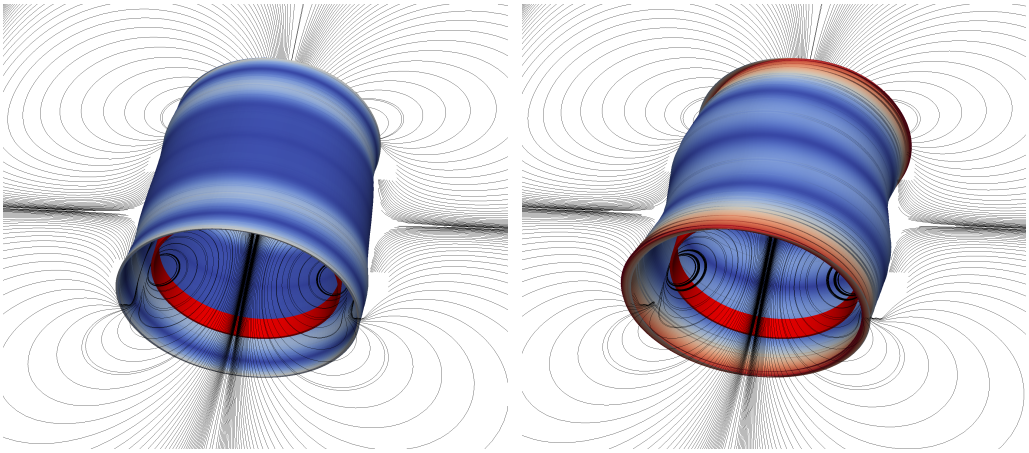

(a) $f = 2000$ Hz.

(b) $f = 3591$ Hz.

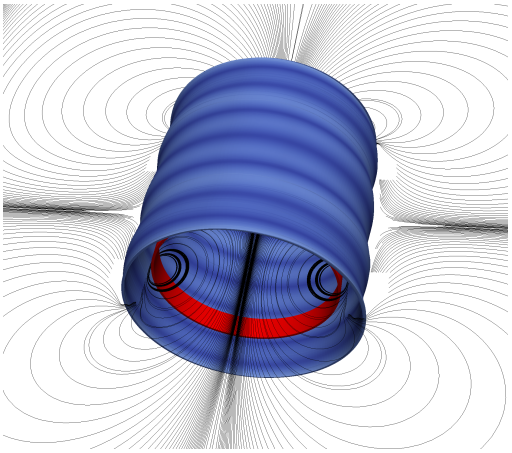

(c) $f = 3871$ Hz.

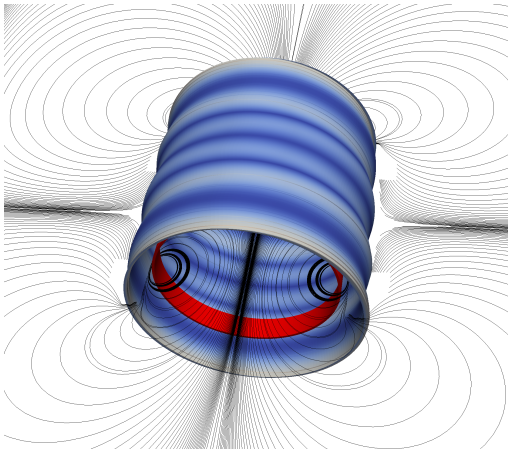

(d) $f = 3956$ Hz.

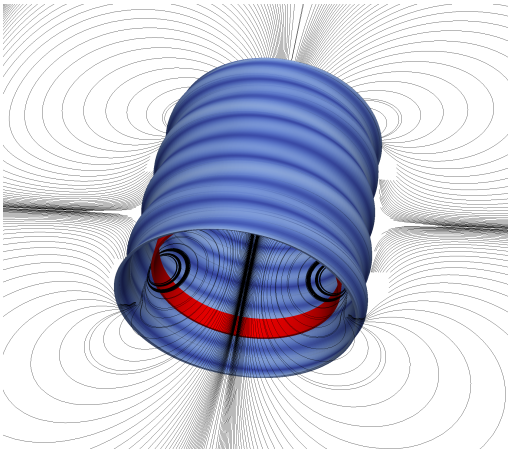

(e) $f = 4281$ Hz.

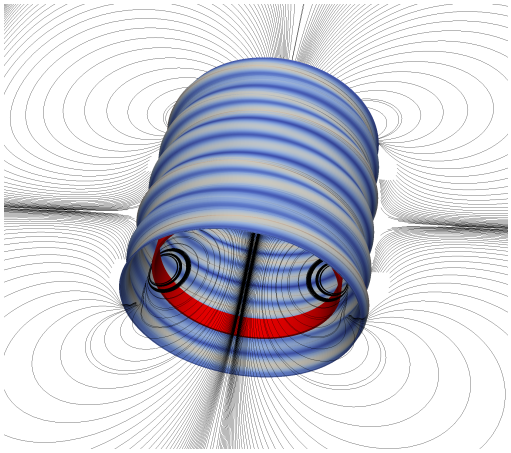

(f) $f = 4881$ Hz.

Figure 16: Test magnet problem; visualisation of the magnetic field $|\boldsymbol{\mathcal{B}}_0^{AC}|$ contour lines on the axisymmetric plane and the magnitude of the displacements $|\boldsymbol{\mathcal{U}}|$ in the OVC shield. Plot of the deformed OVC shield for different frequencies.

Table 2: User-defined parameters for the simulation in Figure 17.

Global PGD parameters				Refined PGD parameters			
I_N	I_{FP}	tol_N	tol_{FP}	I_N	I_{FP}	tol_N	tol_{FP}
20	10	10^{-4}	10^{-2}	40	10	10^{-4}	10^{-2}
Spatial domain Ω_p				Parametric domain Ω_ω			
h	$E_{\Omega_p^C}$	p	α	h_ω	ω_{min}	ω_{max}	tol^{ω}_{split}
0.25	$2.9{\cdot}10^3$	4	100	0.01	1 Hz	5000 Hz	0.05

Ohmic power $P^0_{\Omega^C}$ and kinetic energy $E^k_{\Omega^C}$, see (46).

With this in mind, Figure 17 presents the comparison between the PGD approximation and the full order solution using the user-defined parameters shown in Table 2. These results clearly show a very high accurate PGD approximation that is able to reproduce all the resonance frequencies appearing in the full order model. Whilst a high number of full order solutions are necessary in order to generate this Figure, in the case of the PGD approximation, only the fast online interpolation is needed in real time in order to generate a high number of points in the frequency sweep, being able to achieve a real-time response, see Section 4.4.

6.2 Full magnet problem

The full magnet problem is a more realistic MRI scanner configuration that, similarly to the test magnet problem, consists of three radiation shields in a non conducting domain, see Figure 18. Note that now the three shields, OVC, 77K and 4K, have a more complex geometry consisting in closed cylindrical shells. Again, each shield has different material parameters that cannot be exactly specified due to confidentiality issues. However, the approximate values are $\mu_* \approx 10^{-7}$ H/m, $\gamma_* \approx 10^6$ S/m, $\rho \approx 10^3$ Kg/m^3, $E \approx 10^9$ Pa, $\nu \approx 0.3$. The thickness of each shield is slightly different and it is of the order of a few millimetres. The problem is excited through the current sources $\boldsymbol{J}^{DC}$ and $\boldsymbol{\jmath}^{AC}$ that create a uniform magnetic field of strength $B_0 = \max(||\boldsymbol{B}_0^{DC}|_{r=0}||) = 1.5$ T and a gradient along the $r = 0$ axis of $||\partial \boldsymbol{\mathcal{B}}_0^{AC}|_{r=0}/\partial z|| = 100$ mT/m, respectively. Regarding the boundary conditions, displacements $\boldsymbol{u} = \boldsymbol{u}_D = \boldsymbol{0}$ are fixed at the rear part of each shield (see Figure 18) and the scalar potential is set to $\mathcal{A}_\phi = \mathcal{A}_{\phi,D} = 0$ far away from the conducting objects such that $\boldsymbol{n} \times \boldsymbol{A}^{AC} = \boldsymbol{0}$ on $\partial\Omega$.

6.2.1 Full order model

Before validating and benchmarking the PGD algorithm, the full order solution is presented in this Section. Although this paper focuses on the transient AC problem, it has been

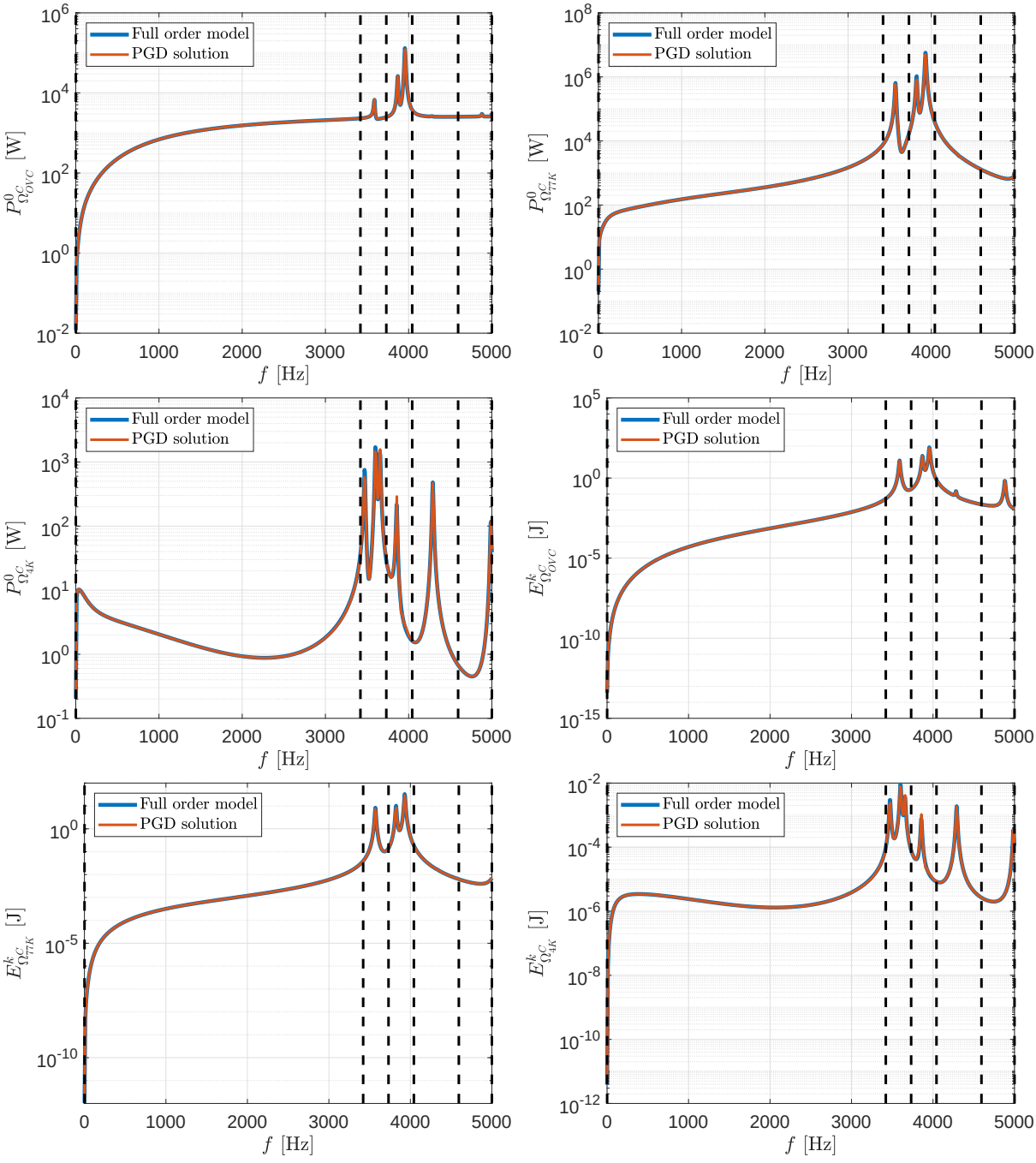

Figure 17: Test magnet problem; comparison between PGD approximation and full order model with a damping coefficient $\alpha = 100$ using 40 PGD modes and 10 ADS iterations for each frequency subdomain. Plot of dissipated power $P^0_{\Omega^C}$ and kinetic energy $E^k_{\Omega^C}$ in the three conducting shields OVC, 77K and 4K.

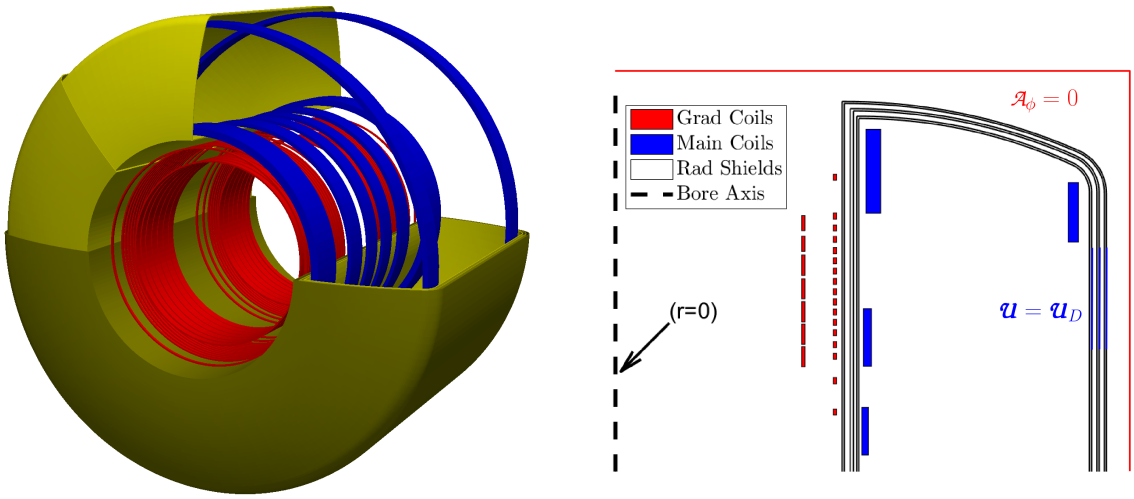

Figure 18: Full magnet problem; geometry description. 3D view (left) and 2D axisymmetric view (right) with components names and boundary conditions.

explained in Section 3.1 that the total solution is the sum of DC and AC stages. It is interesting to observe the solution of both problems as presented in Figure 19, where a mesh of 17.4K triangular elements with $p = 4$ is used. First, the DC problem is solved excited through a static current source that generates a strong static magnetic field which is as uniform as possible on the imaging bore axis ($r = 0$). Figure 19a shows this static solution and how it is indeed fairly uniform in the interior of the MRI scanner. Note that the magnetic field $\boldsymbol{B}_0^{DC}$ is generated in the main coils. In addition, this Figure shows the static magnetic field magnitude in the OVC shield, with maximum values near the set of main coils. Once the static solution is obtained, this will become the initial state of the dynamic problem, which will be solved considering a dynamic current source several orders of magnitude lower than the static one, in this particular case $|\boldsymbol{\jmath}^{AC}|/|\boldsymbol{J}^{DC}| \approx 2\%$. The solution of the AC problem is presented in Figure 19b, where the displacements $|\boldsymbol{\mathcal{U}}|$ are plotted in the OVC shield and the magnitude of the dynamic magnetic field $|\boldsymbol{\mathcal{B}}_0^{AC}|$ is represented through contour lines. In this Figure, it can be seen how the magnetic field is generated in the gradient coils and it is no longer uniform. The displacements have its maximum values in the interior of the MRI device around the gradient coils.

6.2.2 PGD solution

The PGD algorithm has already been validated for the test magnet problem. Now, the robustness and flexibility of the algorithm is assessed with this more challenging geometry: the full magnet problem. With this aim, two different studies will be presented, first a comparison of the PGD approximation and the full order model by computing the absolute error for a given frequency. The second test consists in performing a frequency sweep to

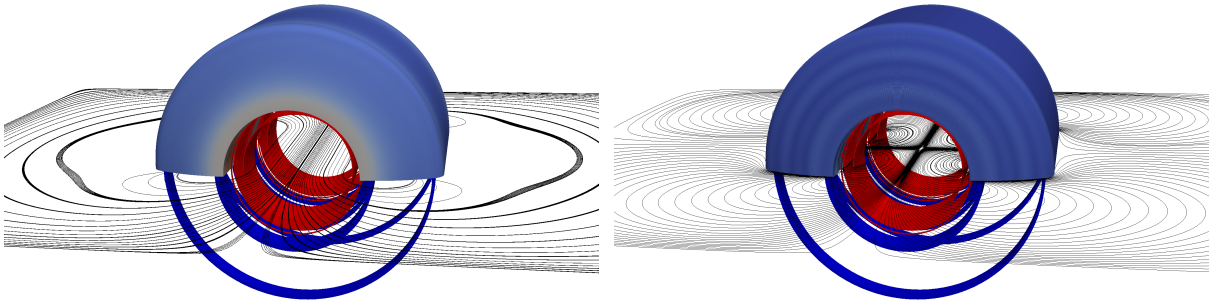

(a) DC problem; visualisation of $|\boldsymbol{B}_0^{DC}|$ in the OVC shield and streamlines.

(b) AC problem; visualisation of $|\boldsymbol{\mathcal{U}}|$ in the OVC shield and streamlines of $|\boldsymbol{\mathcal{B}}_0^{AC}|$.

Figure 19: Full magnet problem; full order solution of both DC and AC problems for a frequency of 1000 Hz.

Table 3: User-defined parameters for the simulation in Figures 20 and 21.

Global PGD parameters				Refined PGD parameters			
I_N	I_{FP}	tol_N	tol_{FP}	I_N	I_{FP}	tol_N	tol_{FP}
10	5	10^{-4}	10^{-2}	20	10	10^{-4}	10^{-2}
Spatial domain Ω_p				Parametric domain Ω_ω			
h	$E_{\Omega_p^C}$	p	α	h_ω	ω_{min}	ω_{max}	tol_{split}^{ω}
0.25	$17.4{\cdot}10^3$	4	50	0.01	1 Hz	5000 Hz	0.05

see if the PGD approximation is able to recover the full order model solution.

Figure 20 shows a comparison between the PGD solution and the full order model for a single frequency of 100 Hz. Two quantities are considered; the magnetic field $|\boldsymbol{\mathcal{B}}_0^{AC}|$ near the gradient coils for electromagnetics and displacements $|\boldsymbol{\mathcal{U}}|$ in the three shields for mechanics. The user-defined parameters used in this simulation are presented in Table 3. Similar conclusions apply to both physics, the PGD solution has a good agreement with the full order model, achieving errors of approximately 1-10%. These results suggest that the PGD solution is a good approximation of the problem considered.

Similarly than for the test magnet problem, the second study consists on a frequency sweep in which the two integrated quantities of interest (46) are computed for every frequency of the sweep. In Figure 21, both quantities, dissipated power and kinetic energy, are presented for each shield in the range [1, 2000] Hz. Again, the parameters used are specified in Table 3. Note that, since the goal is to capture the first resonance modes, the frequency range has been reduced. In the test magnet case, see Figure 17, the resonance

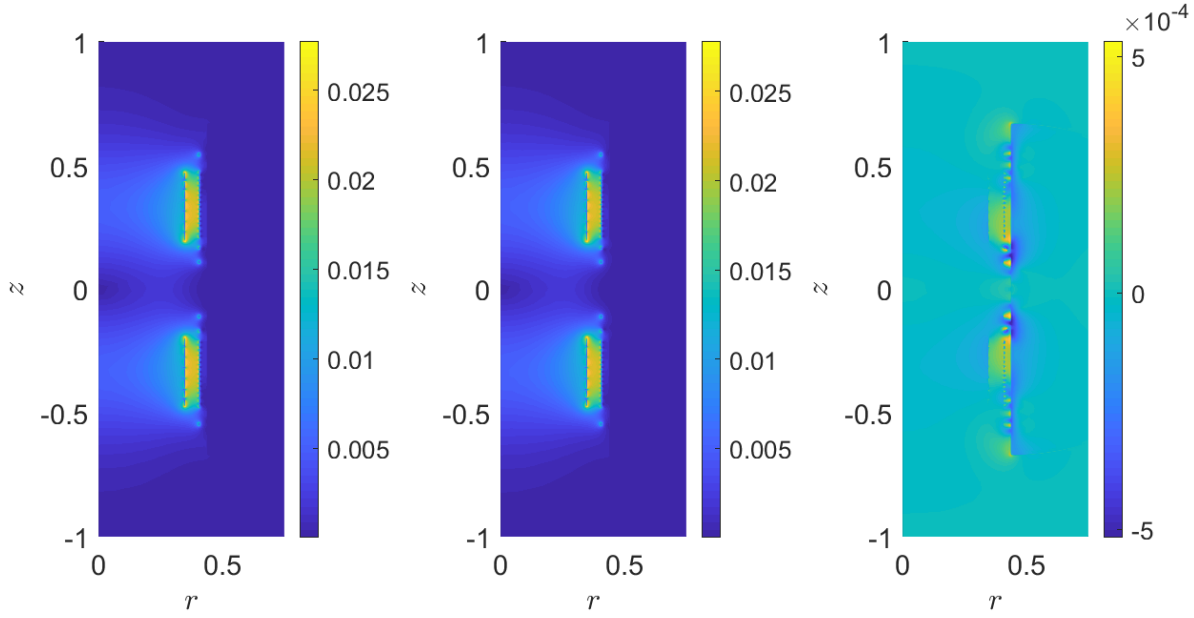

(a) $|\boldsymbol{\mathcal{B}}^{AC}_{0,full}|$ using the full order model.

(b) $|\boldsymbol{\mathcal{B}}^{AC}_{0,PGD}|$ using the PGD approach.

(c) Error $e = |\boldsymbol{\mathcal{B}}^{AC}_{0,full}| - |\boldsymbol{\mathcal{B}}^{AC}_{0,PGD}|$.

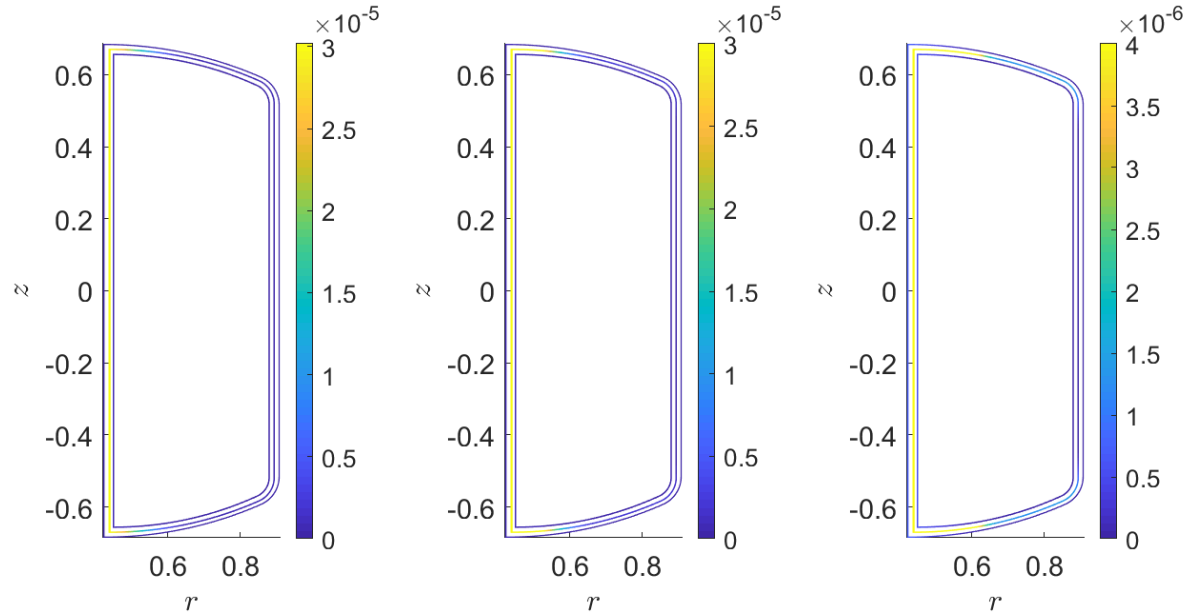

(d) $|\boldsymbol{\mathcal{U}}_{full}|$ using the full order model.

(e) $|\boldsymbol{\mathcal{U}}_{PGD}|$ using the PGD approach.

(f) Error $e = |\boldsymbol{\mathcal{U}}_{full}| - |\boldsymbol{\mathcal{U}}_{PGD}|$.

Figure 20: Full magnet problem; comparison between solutions obtained using the full order model and the PGD approach. Visualisation of $|\boldsymbol{\mathcal{B}}^{AC}_0|$ around the gradient coils and $|\boldsymbol{\mathcal{U}}|$ in the conducting shields for a frequency of 100 Hz.

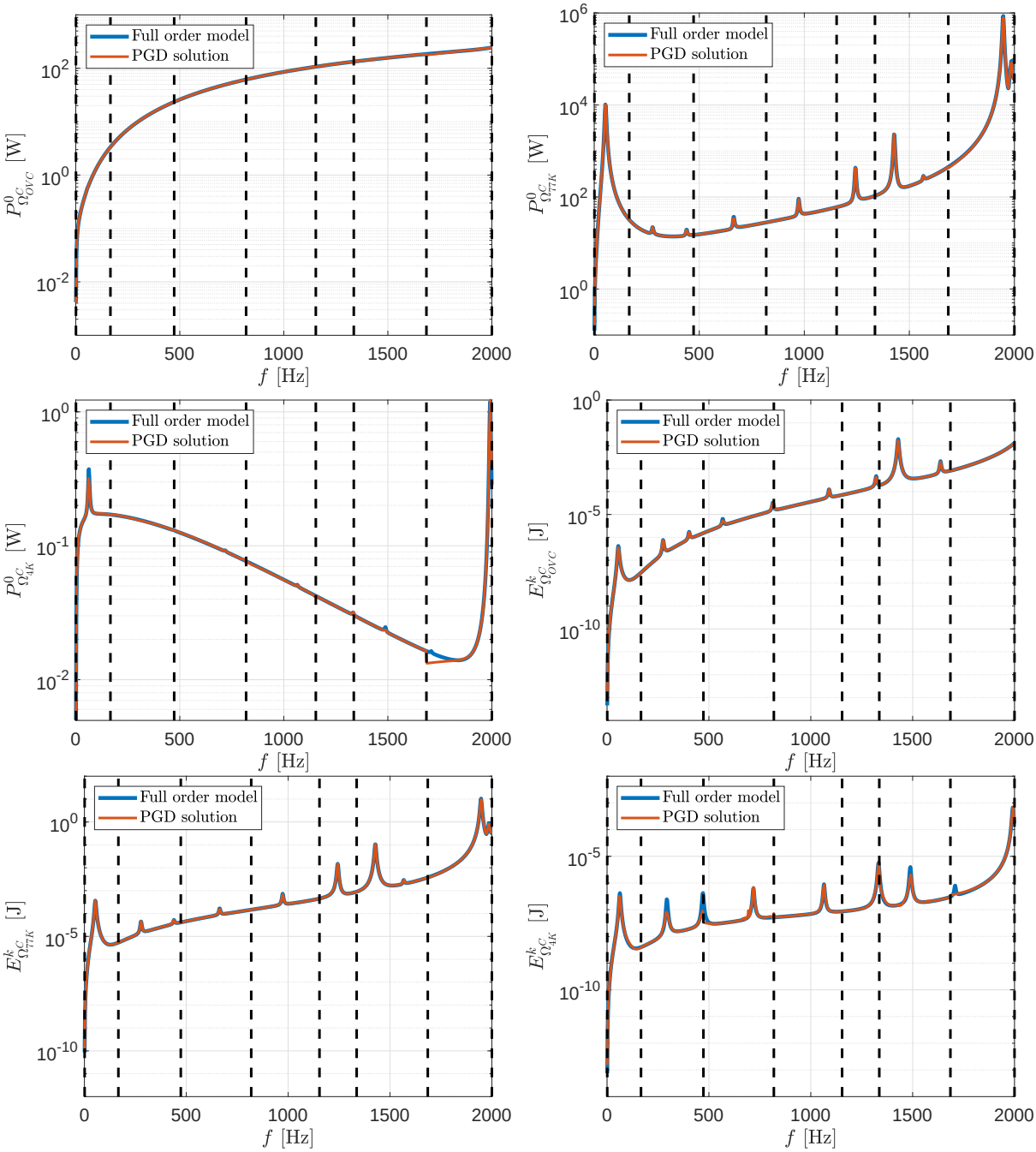

Figure 21: Full magnet problem; comparison between PGD approximation and full order model with a damping coefficient $\alpha = 50$ using 20 PGD modes and 10 ADS iterations for each frequency subdomain. Plot of the dissipated power $P^0_{\Omega^C}$ and kinetic energy $E^k_{\Omega^C}$ in the three conducting shields OVC, 77K and 4K.

Figure 22: On-line PGD application for coupled magneto-mechanical problems with application to MRI scanners. Visualisation of the four tabs; Presentation, Loading PGD, Plotting and Frequency sweep.

phenomenon did not occur until 3500 Hz whereas for this full magnet case, resonance appears throughout the entire frequency range. These differences are due to the more complex geometry of the full magnet that includes closed cylindrical shells. Hence, this more realistic geometry represents a major challenge which is however nicely resolved by the regularised-adaptive PGD algorithm, splitting the frequency domain accordingly and capturing all the singularities accurately.

Finally, a simple Matlab [54] application has been designed to create a user-friendly interface that particularises the high-order parametric solution computed in the offline PGD stage as presented in Figure 6. This PGD app is presented in Figure 22 where four different tabs are displayed. The first one presents the application and its developers. The second one loads a particular precomputed PGD offline solution. The third tab displays the plot of a particular field of interest. Moreover, this tab also offers numerical quantities computed on the fly that are industrially relevant. The last tab offers the possibility to perform a frequency sweep in a range of interest and plot a specific quantity of interest in

one of the conducting components of the problem. The entire interface is based on sliders, numerical boxes, switches and lamps that make the app very user-friendly.

7 Conclusion

This paper has presented a new Reduced Order Modelling Proper Generalised Decomposition (ROM-PGD) method to help speed up the design phase of the next generation of MRI scanners (>7T), improving the optimisation workflow through a real-time, multiple-query, frequency-based enabled online stage. The work focusses on using the external exciting frequency as an additional parameter of the offline higher-dimensional parametric solution permitting frequency spectra for kinetic energy and dissipated Ohmic power to be efficiently queried in the online stage. The paper derives the ROM-PGD methodology for the coupled electro-magneto-mechanical problem of interest and introduces a regularised adaptive methodology to account for the numerical singularities associated with the ill-conditioning of the discrete system in the vicinity of resonant modes. A key advantage of this approach is the fact that the major computational expense takes place during the offline stage, whilst the online stage can be resolved in real-time and through user-friendly app interfaces, such as that shown in the paper. The further consideration of optimisation parameters such as the magnetic conductivity, the strength of the static magnetic field or the thicknesses of the conducting shields constitute the next steps of our work, in the search of a surrogate digital twin model which allows for real-time simulations, thus minimising human intervention.

Acknowledgements

The authors would like to thank the European Commission for the funding received through the Marie Sklodowska-Curie Innovative Training Network AdMoRe with grant number 675919.

References

[1] J. A. Pope, Medical Physics: Imaging, Heinemann, United States, 1999.

[2] A. Brydie, N. Raby, Early MRI in the management of clinical scaphoid fracture, The British Journal of Radiology 76 (905) (2003) 296–300.

[3] A. Savnik, H. Malmskov, H. S. Thomsen, L. B. Graff, H. Nielsen, B. Danneskiold-Samsøe, J. Boesen, H. Bliddal, MRI of the wrist and finger joints in inflammatory joint diseases at 1-year interval: MRI features to predict bone erosions, European Radiology 12 (5) (2002) 1203–1210.

[4] S. J. Matzat, J. van Tiel, G. E. Gold, E. H. Oei, Quantitative MRI techniques of cartilage composition, Quantitative Imaging in Medicine and Surgery 3 (3) (2013) 162.

[5] P. Kozlowski, S. D. Chang, E. C. Jones, K. W. Berean, H. Chen, S. L. Goldenberg, Combined diffusion-weighted and dynamic contrast-enhanced MRI for prostate cancer diagnosis: Correlation with biopsy and histopathology, Journal of Magnetic Resonance Imaging: An Official Journal of the International Society for Magnetic Resonance in Medicine 24 (1) (2006) 108–113.

[6] R. Aarnink, J. Overweg, Magnetic resonance imaging, a success story for superconductivity, Europhysics News 43 (4) (2012) 26–29.

[7] R. H. Hashemi, W. G. Bradley, C. J. Lisanti, MRI: The Basics, Lippincott Williams & Wilkins, United States, 2012.

[8] Siemens Healthineers. Magnetic resonance imaging, https://www.healthcare.siemens.com/magnetic-resonance-imaging, accessed: 20/11/2018 (2018).

[9] G. A. Kerchner, Ultra-high field 7T MRI: a new tool for studying Alzheimer's disease, Journal of Alzheimer's Disease 26 (s3) (2011) 91–95.

[10] P. D. Ledger, J. Peraire, K. Morgan, O. Hassan, N. Weatherill, Adaptive *hp* finite element computations of the scattering width output of Maxwell's equations., International Journal for Numerical Methods in Fluids 43 (2003) 953–978.

[11] A. Buffa, H. Ammari, J.-C. Nédélec, A justification of eddy currents model for the Maxwell equations, SIAM Journal on Applied Mathematics 60 (5) (2000) 1805–1823.

[12] A. A. Rodríguez, A. Valli, Eddy Current Approximation of Maxwell Equations: Theory, Algorithms and Applications, Vol. 4, Springer Science & Business Media, 2010.

[13] S. Kurz, J. Fetzer, G. Lehner, W. M. Rucker, A novel formulation for 3D eddy current problems with moving bodies using a Lagrangian description and BEM-FEM coupling, IEEE Transactions on Magnetics 34 (5) (1998) 3068–3073.

[14] P. D. Ledger, S. Zaglmayr, *hp*-Finite element simulation of three-dimensional eddy current problems on multiply connected domains, Computer Methods in Applied Mechanics and Engineering 199 (49) (2010) 3386–3401.

[15] T. J. R. Hughes, The Finite Element Method: Linear Static and Dynamic Finite Element Analysis, Courier Corporation, United States, 2012.

[16] S. Bagwell, A Numerical Multi-Physics Approach to Understanding MRI Scanners and their Complex Behaviour, Ph.D. thesis, Swansea University, UK (2018).

[17] M. J. Graves, D. G. Mitchell, Body MRI artifacts in clinical practice: a physicist's and radiologist's perspective, Journal of Magnetic Resonance Imaging 38 (2) (2013) 269–287.

[18] K. Krupa, M. Bekiesińska-Figatowska, Artifacts in magnetic resonance imaging, Polish Journal of Radiology 80 (2015) 93.

[19] C. Lalanne, Mechanical Vibration and Shock Analysis, Fatigue Damage, Vol. 4, John Wiley & Sons, 2010.

[20] S. Bagwell, P. D. Ledger, A. J. Gil, M. Mallett, M. Kruip, A linearised hp–finite element framework for acousto-magneto-mechanical coupling in axisymmetric MRI scanners, International Journal for Numerical Methods in Engineering 112 (10) (2017) 1323–1352.

[21] S. Bagwell, P. D. Ledger, A. J. Gil, M. Mallett, Transient solutions to nonlinear acousto-magneto-mechanical coupling for axisymmetric MRI scanner design, International Journal for Numerical Methods in Engineering 115 (2) (2018) 209–237.

[22] M. Rausch, M. Gebhardt, M. Kaltenbacher, H. Landes, Magnetomechanical field computations of a clinical magnetic resonance imaging (MRI) scanner, COMPEL-The International Journal for Computation and Mathematics in Electrical and Electronic Engineering 22 (3) (2003) 576–588.

[23] M. Rausch, M. Gebhardt, M. Kaltenbacher, H. Landes, Computer-aided design of clinical magnetic resonance imaging scanners by coupled magnetomechanical-acoustic modeling, IEEE Transactions on Magnetics 41 (1) (2005) 72–81.

[24] P. D. Ledger, A. J. Gil, R. Poya, M. Kruip, I. Wilkinson, S. Bagwell, Solution of an industrially relevant coupled magneto–mechanical problem set on an axisymmetric domain, Applied Mathematical Modelling 40 (3) (2016) 1959–1971.

[25] T. C. Cosmus, M. Parizh, Advances in whole-body MRI magnets, IEEE Transactions on Applied Superconductivity 21 (3) (2011) 2104–2109.

[26] Siemens Healthineers. Magnetic resonance imaging. Siemens Magnet Technology., https://www.healthcare.siemens.co.uk/magnetic-resonance-imaging/siemens-magnet-technology/macrobert-award, accessed: 05/12/2018 (2018).

[27] D. Amsallem, C. Farhat, Interpolation method for adapting reduced-order models and application to aeroelasticity, AIAA Journal 46 (7) (2008) 1803–1813.

[28] F. Chinesta, A. Huerta, G. Rozza, K. Willcox, Model Reduction Methods, in: E. Stein, R. de Borst, T. J. R. Hughes (Eds.), Encyclopedia of Computational Mechanics Second Edition, Vol. Part 1 Solids and Structures, John Wiley & Sons, Ltd., Chichester, 2017, Ch. 3, pp. 1–36. doi:10.1002/9781119176817.ecm2110.

URL https://onlinelibrary.wiley.com/doi/pdf/10.1002/9781119176817.ecm2110

[29] J. S. Peterson, The reduced basis method for incompressible viscous flow calculations, SIAM Journal on Scientific and Statistical Computing 10 (4) (1989) 777–786.

[30] K. Ito, S. Ravindran, A reduced-order method for simulation and control of fluid flows, Journal of Computational Physics 143 (2) (1998) 403–425.

[31] Y. Liang, H. Lee, S. Lim, W. Lin, K. Lee, C. Wu, Proper orthogonal decomposition and its applications. Part i: Theory, Journal of Sound and Vibration 252 (3) (2002) 527–544.

[32] T. R. Smith, J. Moehlis, P. Holmes, Low-dimensional modelling of turbulence using the proper orthogonal decomposition: a tutorial, Nonlinear Dynamics 41 (1-3) (2005) 275–307.

[33] F. Chinesta, R. Keunings, A. Leygue, The Proper Generalized Decomposition for Advanced Numerical Simulations: A Primer, Springer Science & Business Media, Germany, 2013.

[34] D. Modesto, S. Zlotnik, A. Huerta, Proper generalized decomposition for parameterized helmholtz problems in heterogeneous and unbounded domains: Application to harbor agitation, Computer Methods in Applied Mechanics and Engineering 295 (2015) 127–149.

[35] M. Signorini, S. Zlotnik, P. Diez, Proper generalized decomposition solution of the parameterized helmholtz problem: application to inverse geophysical problems, International Journal for Numerical Methods in Engineering 109 (8) (2017) 1085–1102.

[36] J. M. de Almeida, A basis for bounding the errors of proper generalised decomposition solutions in solid mechanics, International Journal for Numerical Methods in Engineering 94 (10) (2013) 961–984.

[37] R. García-Blanco, D. Borzacchiello, F. Chinesta, P. Diez, Monitoring a PGD solver for parametric power flow problems with goal-oriented error assessment, International Journal for Numerical Methods in Engineering 111 (6) (2017) 529–552.

[38] R. Ibáñez, E. Abisset-Chavanne, F. Chinesta, A. Huerta, Simulating squeeze flows in multiaxial laminates: towards fully 3D mixed formulations, Int. J. Mater. Form. 10 (5) (2017) 653–669. doi:/doi.org/10.1007/s12289-016-1309-4.

[39] P. Díez, S. Zlotnik, A. Huerta, Generalized parametric solutions in Stokes flow, Comput. Methods Appl. Mech. Eng.. 326 (2017) 223–240. doi:10.1016/j.cma.2017.07.016.

[40] C. Ghnatios, F. Masson, A. Huerta, A. Leygue, E. Cueto, F. Chinesta, Proper generalized decomposition based dynamic data-driven control of thermal processes, Computer Methods in Applied Mechanics and Engineering 213 (2012) 29–41.

[41] J. V. Aguado, A. Huerta, F. Chinesta, E. Cueto, Real-time monitoring of thermal processes by reduced-order modeling, International Journal for Numerical Methods in Engineering 102 (5) (2015) 991–1017.

[42] B. Bognet, A. Leygue, F. Chinesta, On the fully 3D simulations of thermoelastic models defined in plate and shell geometries, European Journal of Computational Mechanics/Revue Européenne de Mécanique Numérique 21 (1-2) (2012) 40–51.

[43] S. Zlotnik, P. Díez, D. Modesto, A. Huerta, Proper generalized decomposition of a geometrically parametrized heat problem with geophysical applications, International Journal for Numerical Methods in Engineering 103 (10) (2015) 737–758.

[44] M. Seoane, P. D. Ledger, A. J. Gil, M. Mallett, An accurate and efficient three-dimensional high order finite element methodology for the simulation of magneto-mechanical coupling in MRI scanners, International Journal for Numerical Methods in EngineeringAccepted.

[45] S. Baek, R. Gleason, K. Rajagopal, J. Humphrey, Theory of small on large: potential utility in computations of fluid-solid interactions in arteries, Computer Methods in Applied Mechanics and Engineering 196 (31-32) (2007) 3070–3078.

[46] A. J. Gil, J. Bonet, Finite element analysis of prestressed structural membranes, Finite Elements in Analysis and Design 42 (8-9) (2006) 683–697.

[47] A. J. Gil, Structural analysis of prestressed Saint Venant-Kirchhoff hyperelastic membranes subjected to moderate strains, Computers & structures 84 (15-16) (2006) 1012–1028.

[48] A. J. Gil, J. Bonet, Finite element analysis of partly wrinkled reinforced prestressed membranes, Computational Mechanics 40 (3) (2007) 595–615.

[49] R. Poya, R. Sevilla, A. J. Gil, A unified approach for a posteriori high-order curved mesh generation using solid mechanics, Computational Mechanics 58 (3) (2016) 457–490.

[50] F. Chinesta, P. Ladevèze, Separated representations and PGD-based model reduction, Fundamentals and Applications, International Centre for Mechanical Siences, Courses and Lectures 554.

[51] R. A. Horn, The Hadamard product, in: Proceedings of Symposia in Applied Mathematics, Vol. 40, 1990, pp. 87–169.

[52] J. Bonet, A. J. Gil, R. D. Wood, Nonlinear Solid Mechanics for Finite Element Analysis: Statics, Cambridge University Press, 2016.

[53] J. Schöberl, S. Zaglmayr, High order Nédélec elements with local complete sequence properties, COMPEL-The International Journal for Computation and Mathematics in Electrical and Electronic Engineering 24 (2) (2005) 374–384.

[54] Matlab, the MathWorks, Natick, MA, USA (R2018a).